

FILM COOLING PREDICTIONS ALONG THE TIP AND PLATFORM OF A TURBINE BLADE

Erik M. Hohlfeld

Thesis submitted to the Faculty of the
Virginia Polytechnic Institute and State University
in partial fulfillment of the requirements for the degree of

Master of Science
in
Mechanical Engineering

Dr. K. A. Thole, Chair
Dr. C. L. Dancy
Dr. D. K. Tafti

May 8, 2003
Blacksburg, VA

Keywords: gas turbines, film-cooling, platform, tip gap,
microcircuit, blade heat transfer

© 2003, Erik M. Hohlfeld

FILM COOLING PREDICTIONS ALONG THE TIP AND PLATFORM OF A TURBINE BLADE

Erik M. Hohlfeld

Abstract

Turbine airfoils are exposed to the hottest temperatures in the gas turbine with temperatures typically exceeding the melting point of the blade material. Cooling methods investigated in this computational study included parasitic cooling flow losses, which are inherent to engines, and microcircuit channels. Parasitic losses included dirt purge holes, located along the blade tip, and platform leakage flow, which result from gaps between various turbine components. Microcircuits are a novel cooling technique involving small air passages placed near the airfoil surface to enhance internal cooling. This study evaluated the benefit of external film-cooling flow exhausted from strategically placed microcircuits.

Along the blade tip, predictions showed mid-chord cooling was independent of the blowing from microcircuit exits. The formation of a pressure side vortex was found to develop for most microcircuit film-cooling cases. Significant leading edge cooling was obtained from coolant exiting from dirt purge holes with a small tip gap while little cooling was seen with a large tip gap.

Along the blade platform, the migration of coolant from the front leakage was shown to cool a considerable part of the platform. Several hot spots were predicted along the platform, which were circumvented through the placement of microcircuit channels. Ingestion of hot mainstream gas was predicted along the aft portion of the gutter and agreed with distress exhibited by actual gas turbine engines.

Acknowledgements

The author would like to acknowledge all those who have provided guidance and support both in the completion of this thesis and to my personal development during the last twenty-three years. I would like to acknowledge my project sponsor, Pratt & Whitney for providing the financial backing to make this possible as well as the suggestions from all those in Connecticut including Dr. Frank Cunha. Of course I cannot forget my advisor, Dr. Karen Thole for allowing the Pratt money to trickle down and pay for my graduate education and for providing guidance to me and my fellow Pratt team members. She should also be thanked for giving me enough work to fill the next 350 pages. I would also like to thank Dr. D. K. Tafti and Dr. C. L. Dancey for being part of my committee and reviewing this rather large thesis. My colleagues here at VTEXCCL (Virginia Tech Experimental and Computational Convection Lab) and throughout the department also require acknowledgement as we have had some good times in and out of the lab. It has become customary to acknowledge all of my labmates including Andy, Andrew, Chris, Dan, Eric, Evan, Jeff, Jesse, Joe, Mike, Sachin, Will, and William. Before entering graduate school, I spent four semesters working at NIST (National Institute of Standards and Technology) in Gaithersburg, MD, where I was able to work with some great individuals who taught me so much. I would like to thank all of my co-workers in the Building and Fire Research Lab, particularly the Heat Transfer Group.

Certainly without all of the help and encouragement from family and friends I would not be where I am today. Mom, Dad, Sharon and everyone else, thank you so much. To all those people who I have met, worked with, and spent time with at Virginia Tech it has been great and I leave Blacksburg with only great memories. My six year stay in southwestern Virginia has been a remarkable experience and one that I will miss greatly, but as the saying goes, "All good things must come to an end". I only hope that my future endeavors can be as grand as those of the past. Go Hokies!

Contents

	Page #
Abstract.....	ii
Acknowledgements.....	iii
Nomenclature.....	vi
List of Tables.....	viii
List of Figures.....	ix
1. Introduction.....	1
2. Literature Review.....	14
2.1 Tip Studies.....	15
2.2 Platform Studies.....	25
3. Geometry and Test Matrix.....	56
3.1 Blade Scaling.....	57
3.2 Turbine Blade Tip Simulations: Test Matrix and Geometry.....	59
3.3 Turbine Blade Platform Simulations: Test Matrix and Geometry.....	64
4. Computational Methodology.....	92
4.1 CFD Overview and Methodology	92
4.2 Governing Equations and Solution Methods.....	96
4.3 Meshing Techniques.....	98
4.4 Turbulence and Near Wall Modeling.....	102
4.5 Convergence Criteria, Grid Independence and Adaption.....	105
4.6 Data Analysis Techniques.....	108
5. Tip Simulation Results.....	129
5.1 Geometry 1 – Flat Tip with No Blowing.....	129
5.2 Geometry 2 – Dirt Purge Cavity with No Blowing.....	135
5.3 Geometry 3 - Dirt Purge with Blowing.....	137
5.4 Geometry 4 – Microcircuit and Dirt Purge with Blowing.....	147
6. Predictions of Platform Adiabatic Effectiveness.....	197
6.1 Platform Predictions with No Coolant Injection	198
6.2 Platform Predictions with Leakage Injection	201

6.3 Platform Predictions with Leakage and Microcircuit Injection.....	206
7. Benchmarking.....	244
7.1 Experimental Facility.....	245
7.2 Comparison of Predictions and Measurements for the Tip Studies.....	247
8. Conclusions.....	274
8.1 Tip Blowing Studies.....	274
8.2 Platform Effectiveness Studies.....	276
8.3 Recommendations for Future Work	277
References.....	279
Appendix A.....	285
Appendix B.....	292
Appendix C.....	305
Appendix D.....	345

Nomenclature

A	= area
B_x	= axial chord
C	= true chord of blade
C_p	= pressure coefficient, $C_p = (p - p_{in}) / (\rho U_{in}^2 / 2)$
$C_{p, ex}$	= pressure coefficient based on exit conditions, $C_p = (p - p_{ex}) / (\rho U_{ex}^2 / 2)$
d	= diameter
h	= small tip gap height
H	= large tip gap height
I	= momentum flux ratio, $I = \rho_c U_c^2 / \rho_{in} U_{in}^2$
\dot{m}	= mass flowrate
M	= mass flux ratio, $M = \rho_c U_c / \rho_{in} U_{in}$
P	= blade pitch
P_o, p	= total and static pressures
Re_{in}	= Reynolds number defined as $Re_{in} = C U_{in} / \nu$
s	= surface distance along blade from stagnation
S	= span of blade
T	= temperature
U, V, W	= global, mean streamwise velocity component
u, v, w	= in-plane velocity components
X, Y, Z	= global coordinates defined by blade stagnation
x, y, z	= local coordinate system
V_s	= transformed streamwise velocity, $u \cos \psi_{ms} + v \sin \psi_{ms}$
V_n	= transformed normal velocity, $-u \sin \psi_{ms} + v \cos \psi_{ms}$
V_z	= spanwise velocity, w
V_{in}	= inplane velocity
VR	= velocity ratio
ψ_{ms}	= midspan turning angle, $\tan^{-1}(v_{ms} / u_{ms})$
y^+	= non-dimensional turbulent wall units

Greek

η	= adiabatic effectiveness, $\eta = (T_{in} - T_{aw}) / (T_{in} - T_c)$
Θ	= normalized thermal field, $\theta = (T_{in} - T) / (T_{in} - T_c)$
Δ	= denotes a difference in value
ρ	= density
ν	= kinematic viscosity
θ	= inlet flow angle
ϕ	= blade rotation angle

Subscripts

ave, $\overline{\quad}$	= pitchwise average at a given axial location
ave, $\overline{\overline{\quad}}$	= area average
aw	= adiabatic wall
c	= coolant conditions

cold = coolant conditions
in = value at 1C upstream of blade
ms = value at blade midspan
max = maximum value
 ∞ = mainstream conditions

List of Tables

Table 2.1. Researchers who have studied coolant blowing from the tip region (page 32).

Table 3.1. Geometry and flow conditions for the tip (page 70).

Table 3.2. Geometry, tip gap size and coolant flow for each tip gap geometry considered (page 70).

Table 3.3. Average mass flux, momentum flux and velocity ratios for all blowing cases along the tip (page 71).

Table 3.4. Geometry and flow conditions for the platform (page 71).

Table 3.5. Coolant flowrates used for platform testing (page 72).

Table 3.6. Geometry, front rim configuration, and coolant flows for platform tests (page 72).

Table 3.7. Average mass flux, momentum flux and velocity ratios for all blowing cases along the platform (page 73).

Table 5.1. Tip gap leakage measurements (page 159).

Table 6.1. Summary of leakage flows for three engine configurations: PW4000, PW6000, and ActiveMC (page 215).

List of Figures

Figure 1.1. Diagram of the Brayton Cycle representing a gas turbine engine (page 8).

Figure 1.2. McDonnell XFH-1, Phantom, powered by the Westinghouse J30 turbojet engine (page 8). (courtesy www.mundoavion.com)

Figure 1.3. Schematic diagram of a turbojet engine showing the compressor, combustor and turbine sections (page 9). (courtesy Rolls-Royce, 1992)

Figure 1.4. Lockheed Martin X-35, Joint Strike Fighter, powered by the Pratt and Whitney F-135 turbofan engine, a derivative of the F-119 engine (page 9). (courtesy United States Air Force)

Figure 1.5. Pratt & Whitney's F-119 turbofan engine (page 10). (courtesy Pratt & Whitney)

Figure 1.6. Various cooling methods used within a gas turbine including convective, impingement and film cooling (page 10). (courtesy General Electric Aircraft Engines)

Figure 1.7. Diagram of a single turbine blade with the tip and platform highlighted as well as the dirt purge and various platform leakage locations (page 11). (courtesy Pratt & Whitney)

Figure 1.8a-c. Diagram of a) microcircuit embedded within the blade with part of the blade sheathing removing, b) top view of the blade with the tip sheathing removed showing the microcircuit extending over a large portion of the blade, and c) enlarged view of leading edge region showing the tip gap, shroud, microcircuit and other relevant geometry (page 12).

Figure 1.9a-c. Two turbine blades and one vane: a) turbine stator vane after being removed from an engine with 4,000 flights and 11,000 hours of operation, b) turbine rotor blade after operating in a sand laden environment for 8,200 hours and 4,500 flights, and c) turbine rotor blade before entering an engine and without film cooling holes (page 13).

Figure 2.1a-c. Various flow features around the tip of a turbine blade showing a) blade tip with recessed shroud, b) squealer tip and shroud, and c) flow features over the tip gap (page 33). (Bunker, 2000a)

Figure 2.2a-b. Flow streamlines over the blade tip for a) sharp edge blade tip, and b) smooth edge blade tip (page 34). (Ameri and Bunker, 2000)

Figure 2.3a-c. Predictions of film cooling effectiveness along a flat tip for coolant injected from pressure side holes at tip gap heights of a) 1% of the blade span, b) 1.5% of the blade span, and c) 2.5% of the blade span (page 35). (Acharya, et al, 2002)

Figure 2.4a-c. . Predictions of film cooling effectiveness along the shroud for coolant injected from pressure side holes at tip gap heights of a) 1% of the blade span, b) 1.5% of the blade span, and c) 2.5% of the blade span (page 36). (Acharya, et al, 2002)

Figure 2.5a-b. Predictions of streamlines and velocity magnitude contours through a plane at the mid-chord for blowing ratios of a) $M=0.5$ and b) $M=1.5$ (page 37). (Acharya, et al, 2002)

Figure 2.6a-c. Predictions of film cooling effectiveness along a squealer tip for coolant injected from pressure side holes at tip gap heights of a) 1% of the blade span, b) 1.5% of the blade span, and c) 2.5% of the blade span (page 38). (Acharya, et al, 2002)

Figure 2.7a-d. Four different blade tip geometries studied by Metzger to examine variations in heat transfer coefficients including a) discrete slots, b) round holes, c) pressure side injection, and d) grooved tips (page 39). (Kim, et al, 1995)

Figure 2.8a-d. Typical spanwise film cooling effectiveness results at various locations downstream of the cooling ducts for a) discrete slots, b) round holes, c) pressure side injection, and d) grooved tips (page 40). (Kim, et al, 1995)

Figure 2.9a-b. Film cooling hole configuration used by Kim and Metzger to look at cooling effectiveness and heat transfer coefficients shown from a) top and b) side views (page 41). (Kim and Metzger, 1995)

Figure 2.10a-b. Film cooling effectiveness measurements a) shown downstream of film cooling slots, and b) averaged across the span for a blowing ratio of $M=0.5$ at three different Reynolds numbers (page 42). (Kim and Metzger, 1995)

Figure 2.11a-c. Spanwise averaged effectiveness for a) $Re=15,000$ at four blowing ratios, b) $Re=30,000$ at three blowing ratios, and c) $Re=45,000$ at three blowing ratios (page 43). (Kim and Metzger, 1995)

Figure 2.12a-b. Film-cooling configurations shown a) with a squealer tip (Kwak and Han, 2002b) and b) flat tip (Kwak and Han, 2002a) (page 44).

Figure 2.13a-c. Film cooling effectiveness contours for tip blowing over a flat tip having a 1.5% tip gap with blowing ratios of a) $M=0.5$, b) $M=1$, and c) $M=2$ (page 45). (Kwak and Han, 2002a)

Figure 2.14a-c. Film cooling effectiveness contours for tip and pressure side blowing over a flat tip having a 1.5% tip gap with blowing ratios of a) $M=0.5$, b) $M=1$, and c) $M=2$ (page 45). (Kwak and Han, 2002a)

Figure 2.15a-b. Film cooling effectiveness contours for tip blowing over a squealer tip having a 1.5% tip gap with blowing ratios of a) $M=1$, and b) $M=2$ (page 46). (Kwak and Han, 2002b)

Figure 2.16a-b. Film cooling effectiveness for tip and pressure side blowing over a squealer tip having a 1.5% tip gap with blowing ratios of a) $M=1$, and b) $M=2$ (page 46). (Kwak and Han, 2002b)

Figure 2.17. Turbine flow patterns as defined by a) Langston [1980], b) Sharma and Butler [1987], and c) Goldstein [1988] (page 47).

Figure 2.18. Cooling holes located upstream of first stage turbine vane as studied by Oke (page 48). (Oke, et al, 2000)

Figure 2.19. Upstream slot configuration for tests run by Burd (page 49). (Burd, et al, 2000)

Figure 2.20a-b. Diagram of experimental test configuration for Colban and Tholes slot and film cooling work oriented a) looking down at film-cooling holes, dilution jets and slot and b) detailed cross-sectional view of slot configuration (page 49). (Colban and Thole, 2003)

Figure 2.21. Step configuration computationally examined by Stitzel and experimentally tested by Colban showing ingestion into the backward facing step (page 50). (Stitzel, 2001)

Figure 2.22a-b. Views of a) experimental test facility, and b) detailed blade geometry (page 51). (Wang, et al, 1997)

Figure 2.23. Proposed flow patterns within a turbine blade cascade (page 52). (Wang, et al, 1997)

Figure 2.24a-b. Contours of Stanton number along the endwall for the rotor blade geometry (page 53). (Hermanson, et al, 2002)

Figure 2.25. Top view of the experimental test section showing flow control schemes: location of endwall fence as used by Chung and Simon (1993); location of upstream jets (1-5) and location of optimized boundary layer fence (page 53). (Anapu, et al, 2000)

Figure 2.26. Cooling flow injection chambers for radial cooling, impingement cooling and root injection (page 54). (McLean, et al, 2001a, 2001b)

Figure 2.27. Realistic engine leakage flows in a first stage turbine blade (page 55). (courtesy Pratt and Whitney, 2002)

Figure 3.1a-c. Turbine blade shown from three different views including a) side, b) front, and c) isometric (page 74).

Figure 3.2a-b. Important geometric features within a turbine blade including pitch, axial chord, true chord, flow entrance angle, and blade angle for a) tip geometry, and b) platform geometry (page 75).

Figure 3.3. Two different designs for a turbine blade tip cross-section with the high-speed (engine) blade shown in blue and the low-speed (experimental) blade shown in red (page 76).

Figure 3.4. Cross-section of the tip region of a turbine blade showing the tip leakage in relation to the microcircuit and dirt purge cooling (page 77).

Figure 3.5. Dirt purge geometry showing an isometric top view on the left and a side view with the pressure side sheathing removed (page 77).

Figure 3.6a-c. Images of the tip microcircuit geometry from a) top view and b-c) two isometric views looking at the side from above and below the microcircuit (page 78).

Figure 3.7. Tip microcircuit numbering scheme for referencing various flow ducts with microcircuit exits numbered 1-16 and the dirt purge holes 17 and 18 (page 78).

Figure 3.8a-c. Microcircuit and dirt purge shown within a blade looking from a) an isometric view, b) top view and c) side view. Part of the side sheathing removed has been removed to allow internal views (page 79).

Figure 3.9a-c. Four different blade geometries that were studied for tip computations which include a) flat tip, b) dirt purge cavity within tip, c) dirt purge cavity with blowing, and d) microcircuit and dirt purge with blowing (page 80).

Figure 3.10. Non-dimensional cross section of the tip geometry showing microcircuit and dirt purge locations where the horizontal and vertical planes have divided by the axial chord and pitch, respectively (page 81).

Figure 3.11. Exit area of each tip microcircuit and dirt purge hole when compared to the entire coolant flow area (page 82).

Figure 3.12. Schematic diagram of a first stage turbine rotor blade with upstream and downstream stator vanes. Gutter and rim leakage flows are shown in their relative positions (page 83).

Figure 3.13. Various leakage flows throughout the platform geometry. Each has been assigned a reference number and a unique color (page 84).

Figure 3.14a-e. Five different blade geometries were studied for hub computations including a) baseline – no fillet, b) baseline – fillet, c) microcircuit only, d) front, aft and featherseal leakage, and e) front, aft and featherseal leakage combined with microcircuit flow cooling (page 85).

Figure 3.15. Isometric view of the platform geometry showing featherseal leakage (orange), front rim leakage (pink and yellow), aft rim leakage (violet) and microcircuit ducts (green) with the blade fillet (blue) (page 86).

Figure 3.16a-d. Images of the two platform microcircuits looking at a) top view of suction side circuit, b) isometric view of suction side circuit, c) top view of pressure side circuit, and d) isometric view of pressure side circuit (page 87).

Figure 3.17. Side and top view of the platform front rim design with a backward facing step (page 88).

Figure 3.18. Side and top view of the platform aft rim design (page 89).

Figure 3.19. Gutter geometry and microcircuit locations shown on a non-dimensional plot with microcircuit exhausts shown in red, gutter leakage as dark green and the step overhang location shown as light green (page 90).

Figure 3.20. Exit area of each hub microcircuit and leakage gap when compared to the entire coolant flow area. These numbers correspond to the geometry of Figure 3.13 (page 91).

Figure 4.1a-b. Boundary conditions placed on the a) tip models and b) platform models (page 114).

Figure 4.2a-b. Comparison of the pressure distributions around the a) tip geometry and b) platform geometry, for a two-dimensional model with various meshes sizes and boundary conditions (page 115).

Figure 4.3. Pressure distribution for a two-dimensional inviscid model as compared to the pressure distribution at the mid-span for three-dimensional models showing there are no tip gap effects at the mid-span (page 116).

Figure 4.4. Depiction of the various volumes that were used for tip meshing including the microcircuits, dirt purge, plenum, transition, tip and passage volumes (page 117).

Figure 4.5. Depiction of the various volumes that were used for platform meshing including the front passage, aft passage, high passage and endwall volumes (page 118).

Figure 4.6. Contours of velocity magnitude showing the velocity profile is unaffected by the blade one chord length upstream of the stagnation location (page 119).

Figure 4.7 a-d. Meshing around the a) blade and microcircuit ducts, b) plenum and dirt purge cavity, c) microcircuit, and d) blade tip (page 120).

Figure 4.8. Two types of boundary layer modeling are possible with Fluent: wall functions and near-wall modeling (page 121).

Figure 4.9. Typical residual convergence for a tip model (page 121).

Figure 4.10. Laterally averaged adiabatic effectiveness showing the variation between models run with 1.2, 1.65 and 2.0 million cells (page 122).

Figure 4.11a-c. Cell equiangle and equivolume skewness for a) two-dimensional case, b) three-dimensional case with dirt purge blowing and c) three-dimensional case with microcircuit and dirt purge blowing (page 123).

Figure 4.12a-b. Two-dimensional tip geometry before and after a grid adaption, showing the additional cells around the tip surface (page 124).

Figure 4.13a-b. Meshing procedures employed by Fluent to add additional cells to the flow domain including a) hanging node adaption and b) the division of triangular and quadrilateral elements (page 124).

Figure 4.14. Location of suction side (SS) and pressure side (PS) data planes relative the position of the blade for the tip geometry (page 125).

Figure 4.15. Location of suction side (SS) and pressure side (PS) data planes relative the position of the blade for the platform geometry (page 126).

Figure 4.16. Velocity transformation process to visualize secondary flows within the flow passage going from global X, Y, Z, U, V, W coordinates to local streamwise and local normal velocity components (page 127).

Figure 4.17. Process by which data was extracted and laterally averaged effectiveness was calculated. Step 1 shows the division of the domain into multiple sections and Step 2 shows the range of the data points being considered in the averaging process (page 128).

Figure 5.1. Predicted pressure contours along the blade tip and shroud for a flat tip blade with no blowing for small and large tip gaps (page 160).

Figure 5.2a-b. Static pressure distributions and velocity vectors in a plane cut through the tip gap near the mid-chord (page 161).

Figure 5.3a-f. Non-dimensional velocity plotted in a plane placed through the middle of a a) small tip gap with a flat tip, b) large tip gap with a flat tip, c) small tip gap with 0.29% dirt purge blowing, d) large tip gap with 0.29% blowing, e) small tip gap with

1.5% microcircuit and dirt purge blowing, and f) large tip gap with 1.5% microcircuit and dirt purge blowing (page 162).

Figure 5.4a-e. Streamlines released from 1.5 tip gap heights below the shroud that are colored by the non-dimensional spanwise velocity component for a) a small tip gap with a flat blade tip, b) a large tip gap with a flat blade tip, c) a small tip gap and non-flowing purge holes, d) a large tip gap and non-flowing purge holes, and e) two planes set-up along the tip to measure tip leakage flow with the placement based on streamlines (page 163).

Figure 5.5a-d. Secondary flow vectors along a suction side plane (SS6) defined as being normal to the blade at an axial chord location of 94% for a) a small gap and flat tip, b) large gap and flat tip, c) small gap and non-flowing purge cavity and d) large gap and non-flowing purge cavity (page 164).

Figure 5.6a-d. Secondary flow vectors along a pressure side plane (PS2) defined as being normal to the blade at an axial chord location of 30% for a) a small tip gap and flat tip, b) large tip gap and flat tip, c) small tip gap and non-flowing purge cavity and d) large tip gap and non-flowing purge cavity (page 165).

Figure 5.7a-d. Velocity vectors and velocity magnitude shown in a plane cut through the leading edge region of the tip gap where the dirt purge would be located for a) a small gap with flat tip, b) large gap with flat tip, c) small gap and non-blowing dirt purge, d) large gap and non-blowing dirt purge (page 166).

Figure 5.8. Predicted pressure contours along the blade tip and shroud for a non-flowing dirt purge cavity with small and large tip gaps (page 167).

Figure 5.9. Predicted pressure contours along the blade tip and shroud for a dirt purge cavity and small tip gap with blowing ratios of 0.05%, 0.10%, 0.19%, 0.29%, and 0.38% core flow (page 168).

Figure 5.10. Predicted pressure contours along the blade tip and shroud for a dirt purge cavity and large tip gap with blowing ratios of 0.05%, 0.10%, 0.19%, 0.29%, and 0.38% core flow (page 169).

Figure 5.11a-b. Streamlines released from 1.5 tip gap heights below the shroud that are colored by the non-dimensional spanwise velocity component for dirt purge blowing with a) a small tip and 0.29% blowing, and b) large tip and 0.29% blowing (page 170).

Figure 5.12a-b. Secondary flow vectors along a suction side plane (SS6) defined as being normal to the blade at an axial chord location of 94% for a) a small tip gap and 0.29% blowing, and b) large tip gap and 0.29% blowing (page 171).

Figure 5.13a-d. Streamlines colored by non-dimensional temperature released from the dirt purge for a a) small tip gap and 0.29% blowing, b) large tip gap and 0.29% blowing, c) small tip gap and 0.19% blowing and d) large tip gap and 0.19% blowing (page 172).

Figure 5.14a-b. Secondary flow vectors along a pressure side plane (PS2) defined as being normal to the blade at an axial chord location of 30% for a a) small tip and 0.29% blowing, and b) large tip and 0.29% blowing (page 173).

Figure 5.15. Predictions of adiabatic effectiveness along the tip and shroud for the small tip gap with dirt purge blowing at ratios of 0.05%, 0.10%, 0.19%, 0.29%, and 0.38% core flow (page 174).

Figure 5.16. Predictions of adiabatic effectiveness along the tip and shroud for the large tip gap with dirt purge blowing at ratios of 0.05%, 0.10%, 0.19%, 0.29% and 0.38% core flow (page 175).

Figure 5.17a-d. Cross-sectional view of the dirt purge for a a) small tip with 0.29% blowing, b) large tip with 0.29% blowing, c) small tip with 0.19% blowing, and d) large tip gap with 0.19% blowing (page 176).

Figure 5.18. Comparison of pitchwise-averaged effectiveness along the tip for the small tip gap with dirt purge blowing (page 177).

Figure 5.19. Comparison of pitchwise-averaged effectiveness along the tip for the large tip gap with dirt purge blowing (page 177).

Figure 5.20. Comparison of pitchwise-averaged effectiveness along the shroud for the small tip gap with dirt purge blowing (page 178).

Figure 5.21. Comparison of pitchwise-averaged effectiveness along the shroud for the large tip gap with dirt purge blowing (page 178).

Figure 5.22. Area-averaged effectiveness over the tip and shroud plotted against the dirt purge coolant mass flow rate (page 179).

Figure 5.23. Microcircuit and dirt purge numbering scheme (page 179).

Figure 5.24. Comparison of flow distribution within the microcircuit. Numbers 1-16 represent the microcircuit holes with 17 and 18 the dirt purge holes (page 180).

Figure 5.25. Momentum flux ratio for microcircuit cooling ducts at 1.0% and 1.5% cooling flow which is independent of tip gap height. Numbers 1-16 represent the microcircuit holes with 17 and 18 the dirt purge holes (page 180).

Figure 5.26. Predicted pressure contours along the blade tip and shroud for a microcircuit and dirt purge with a small tip gap and blowing ratios of 0.5%, 1.0%, 1.5%, and 2.0% core flow. High pressure is noted when values exceed the scale (page 181).

Figure 5.27. Predicted pressure contours along the blade tip and shroud for a microcircuit and dirt purge with a large tip gap and blowing ratios of 0.5%, 1.0%, 1.5%, and 2.0% core flow. High pressure is noted when values exceed the scale (page 182).

Figure 5.28a-d. Streamlines colored by non-dimensional temperature that are released from the plenum within the blade cavity before exiting the main flow via microcircuit and dirt purge ducts for a a) small tip and 1.5% blowing, b) large tip and 1.5% blowing, c) small tip and 1.0% blowing and d) large tip and 1.0% blowing (page 183).

Figure 5.29a-b. Secondary flow vectors with contours of temperature plotted along a pressure side plane (PS2) defined as being normal to the blade at an axial chord location of 30% for microcircuit cooling with a a) small tip gap and 1.5%, and b) large tip gap and 1.5% blowing (page 184).

Figure 5.30a-b. Secondary flow vectors with contours of temperature plotted along a suction side plane (SS6) defined as being normal to the blade at an axial chord location of 94% for microcircuit cooling with a a) small tip gap and 1.5%, and b) large tip gap and 1.5% blowing (page 185).

Figure 5.31a-b. Streamlines released from 1.5 tip gap heights below the shroud that are colored by the non-dimensional spanwise velocity component for microcircuit and dirt purge coolant with a a) small tip and 1.5% blowing, and b) large tip and 1.5% blowing (page 186).

Figure 5.32. Predicted adiabatic effectiveness contours along the blade tip and shroud for a microcircuit and dirt purge with a small tip gap and blowing ratios of 0.5%, 1.0%, 1.5% and 2.0% core flow (page 187).

Figure 5.33. Predicted adiabatic effectiveness contours along the blade tip and shroud for a microcircuit and dirt purge with large tip gap and blowing ratios of 0.5%, 1.0%, 1.5% and 2.0% core flow (page 188).

Figure 5.34. Predicted adiabatic effectiveness contours along the blade tip for small and large tip gaps with microcircuit blowing ratios of 0.5%, 1.0%, 1.5% and 2.0% core flow. The arrows around the blade indicate the microcircuit exits (page 189).

Figure 5.35a-d. Cross-sectional view of the dirt purge cavity for microcircuit and dirt purge cooling with a small tip gap and a) 0.5%, b) 1.0%, c) 1.5%, and d) 2.0% blowing (page 190).

Figure 5.36a-d. Cross-sectional view of the dirt purge cavity for microcircuit and dirt purge cooling with a large tip gap and a) 0.5%, b) 1.0%, c) 1.5%, and d) 2.0% blowing (page 191).

Figure 5.37a-d. Mid-chord blade cross-section through a microcircuit duct showing the coolant path for associated with a small tip gap and a) 0.5%, b) 1.0%, c) 1.5%, and d) 2.0% blowing (page 192).

Figure 5.38a-d. Mid-chord blade cross-section through a microcircuit duct showing the coolant path for a large tip gap and a) 0.5%, b) 1.0%, c) 1.5%, and d) 2.0% blowing (page 193).

Figure 5.39. Comparison of pitchwise-averaged effectiveness along the tip for the small tip gap with microcircuit and dirt purge blowing (page 194).

Figure 5.40. Comparison of pitchwise-averaged effectiveness along the tip for the large tip gap with microcircuit and dirt purge blowing (page 194).

Figure 5.41. Comparison of pitchwise-averaged effectiveness along the shroud for the small tip gap with microcircuit and dirt purge blowing (page 195).

Figure 5.42. Comparison of pitchwise-averaged effectiveness along the shroud for the large tip gap with microcircuit and dirt purge blowing (page 195).

Figure 5.43. Area-averaged effectiveness along the tip and shroud plotted against coolant mass flow rates (page 196).

Figure 6.1. Various leakage flows throughout the platform geometry. Each has been assigned a reference number and a unique color (page 216).

Figure 6.2. Isometric view of the platform geometry showing featherseal leakage (orange), front rim leakage (pink and yellow), aft rim leakage (violet) and microcircuit ducts (green) with the blade fillet (blue) (page 217).

Figure 6.3. Secondary flow planes around the platform defined as being normal to the blade with three pressure side (PS) planes and five suction side (SS) planes (page 218).

Figure 6.4a-b. Secondary flow vectors along a pressure side plane (PS2) defined as being normal to the blade at an axial location of 57% of the axial chord for a a) baseline case with no fillet and b) baseline case with fillet (page 219).

Figure 6.5a-b. Secondary flow vectors along a suction side plane (SS4) defined as being normal to the blade at an axial location of 96% of the axial chord for a a) baseline case with no fillet and b) baseline case with fillet (page 220).

Figure 6.6a-b. Secondary flow vectors with contours of non-dimensional temperatures for a case with leakage flows in the a) PS2 plane defined as being normal to the blade at an axial location of 57% of the axial chord, b) SS4 plane defined as being normal to the blade at an axial location of 96% of the axial chord (page 221).

Figure 6.7a-c. Contours of adiabatic effectiveness along the turbine blade platform for three different cases of leakage cooling flow. For each case leakage coolant flow is constant (corresponding to ActiveMC leakage) with the exception of aft leakage which is varied between a) 1.5%, b) 2.0% and c) 2.5% of the core flow (page 222).

Figure 6.8. Pitchwise-averaged effectiveness along the platform for cases with constant leakage flows (corresponding to ActiveMC leakage) with the exception of the aft leakage leakage which varied in each case between a) 1.5%, b) 2.0% and c) 2.5% of the core flow (page 223).

Figure 6.9a-c. Contours of non-dimensional temperature taken along the platform at the exit of the aft rim showing the variations in fluid temperatures between a) 1.5%, b) 2.0% and c) 2.5% aft leakage flow (page 224).

Figure 6.10a-c. Non-dimensional temperature within the aft gutter showing hot gases ingested into the gutter for blowing ratios of a) 1.5%, b) 2.0%, and c) 2.5% core flow (page 225).

Figure 6.11. Pressure contours along the platform for a case of ActiveMC leakage flow (page 226).

Figure 6.12a-c. Pressure contours around a plane cut through the middle of the aft gutter for ActiveMC leakage flows and variable aft leakage flow of a) 1.5%, b) 2.0%, and c) 2.5% core flow (page 227).

Figure 6.13a-c. Contours of adiabatic effectiveness along the platform for combined microcircuit and leakage cooling with engine flows relating to the a) ActiveMC, b) PW6000, and c) PW4000 (page 228).

Figure 6.14a-c. Contours of adiabatic effectiveness along the platform for combined microcircuit and leakage cooling with ActiveMC leakage and variations in the microcircuit flow corresponding to a) 0.24%, b) 0.48%, and c) 0.96% core flow (page 229).

Figure 6.15a-b. Contours of adiabatic effectiveness along the platform for the a) ActiveMC flows, and b) ActiveMC flow with just microcircuit cooling (page 230).

Figure 6.16. Pitchwise-averaged adiabatic effectiveness along the platform for combined microcircuit and leakage cooling with engine flows relating to the ActiveMC, PW6000, and PW4000 (page 231).

Figure 6.17. Pitchwise-averaged effectiveness along the platform for the ActiveMC leakage with variations in the microcircuit flow rates corresponding to 0.24%, 0.48% and 0.96% core flow (page 231).

Figure 6.18. Pitchwise-averaged effectiveness along the platform for the ActiveMC, and ActiveMC with just microcircuit cooling (page 232).

Figure 6.19. Pitchwise-averaged effectiveness along the platform for the ActiveMC, and ActiveMC without microcircuit cooling (page 232).

Figure 6.20a-c. Secondary flow vectors and contours of non-dimensional temperature along a pressure side plane (PS2) defined as being normal to the blade at an axial location of 57% for engine flowrates for a(n) a) ActiveMC without microcircuit injection, b) ActiveMC, c) PW6000, and d) PW4000 (page 233).

Figure 6.21a-d. Secondary flow vectors and contours of non-dimensional temperature along a pressure side plane (SS4) defined as being normal to the blade at an axial location of 96% for a(n) a) ActiveMC without microcircuit injection, b) ActiveMC, c) PW6000, and d) PW4000 engines (page 234).

Figure 6.22. Contours of non-dimensional temperature with velocity vectors within the aft gutter showing the ingestion of hot mainstream gases for engine flowrates corresponding to the a) ActiveMC, b) PW6000, and c) PW4000 (page 235).

Figure 6.23. Pressure contours around a plane cut through the middle of the aft gutter for a) ActiveMC, b) PW6000, and c) PW4000 leakage flows as depicted by Table 6.1 (page 236).

Figure 6.24. Streamlines colored by non-dimensional temperature released within the aft gutter just below the turbine platform. The streamlines exit through the aft rim and not the gutter (ActiveMC configuration shown) (page 237).

Figure 6.25. Contours of non-dimensional temperature with velocity vectors cut through the backward facing step at the leading edge of the turbine platform for cases three different cooling cases with the a) ActiveMC, b) PW6000, and c) PW4000 (page 238).

Figure 6.26. Contours of non-dimensional temperature in a plane located at the exit of the backward facing step to look for hot gas ingestion for cases with a) ActiveMC, b) PW6000, and c) PW4000 cooling flows (page 239).

Figure 6.27. Streamlines colored by non-dimensional temperature released upstream of the backward facing step along the platform to study any flow patterns that may develop and cause ingestion (ActiveMC configuration shown) (page 240).

Figure 6.28. Contours of non-dimensional temperature in a plane cut through the featherseal gap for cases with a) ActiveMC without microcircuits, b) ActiveMC, c) PW6000, and d) PW4000 (page 241).

Figure 6.29. Streamlines released from the featherseal plenum showing the trajectory of the flow that exits from the featherseal with the ActiveMC configuration (page 242).

Figure 6.30. Area-averaged adiabatic effectiveness along the platform plotted against coolant flows for various cases (page 243).

Figure 7.1. Diagram of VT ExCCL experimental wind tunnel facility (page 258).

Figure 7.2. Tip test section geometry showing the IR camera window and the flow control mechanisms including the side gates, and flexible outer wall (page 259). (Couch, 2003)

Figure 7.3. Platform test section showing the flexible outer wall and outer gates as well as several leakage gaps and microcircuit locations (page 259). (Ranson, 2004)

Figure 7.4. Photographs of the tip test section showing a view from a) upstream of the blades looking at the two passages and the black experimental tip, and b) behind the test section showing the flexible outer walls and blade adjustment mechanism (page 260).

Figure 7.5. Computational data used to place pressure taps within the experimental facility and record pressure contours (page 261).

Figure 7.6. Experimental assembly of IR images. Four separate IR camera images are shown after the calibration process before being assembled into one final image and cleaned up for final presentation (page 261). (Christophel, 2003)

Figure 7.7. Computational (top) and experimental (bottom) baseline pressure contours taken from a flat tip with a small and large tip gap (page 262).

Figure 7.8. Computational (top) and experimental (bottom) pressure contours taken with dirt purge blowing levels of 0.10%, 0.19%, 0.29% and 0.38% core flow for a small tip gap (page 263).

Figure 7.9. Computational (top) and experimental (bottom) pressure contours taken with dirt purge blowing levels of 0.10%, 0.19%, 0.29% and 0.38% core flow for a large tip gap (page 264).

Figure 7.10. Computational (top) and experimental (bottom) adiabatic effectiveness contours taken with dirt purge blowing levels of 0.10%, 0.19%, 0.29%, 0.38% core flow for a small tip gap (page 265).

Figure 7.11. Computational (top) and experimental (bottom) adiabatic effectiveness contours taken with dirt purge blowing levels of 0.10%, 0.19%, 0.29%, 0.38% core flow for a large tip gap (page 266).

Figure 7.12. Computational (top) and experimental (bottom) pressure contours taken with microcircuit blowing levels of 0.5%, 1.0%, 1.5% and 2.0% core flow for a small tip gap. Maximum pressure inside and outside the dirt purge is noted when the range is exceeded (page 267).

Figure 7.13. Computational (top) and experimental (bottom) pressure contours taken with microcircuit blowing levels of 0.5%, 1.0%, 1.5%, 2.0% core flow for a large tip gap. Maximum pressure inside and outside the dirt purge is noted when the range is exceeded (page 268).

Figure 7.14. Computational (top) and experimental (bottom) adiabatic effectiveness contours taken with microcircuit blowing levels of 0.5%, 1.0%, 1.5%, 2.0% core flow for a small tip gap. Arrows indicate the location of the microcircuit ducts (page 269).

Figure 7.15. Computational (top) and experimental (bottom) adiabatic effectiveness contours taken with microcircuit blowing levels of 0.5%, 1.0%, 1.5%, 2.0% core flow for a large tip gap. Arrows indicate the location of the microcircuit ducts (page 270).

Figure 7.16. Computational and experimental pitchwise-averaged adiabatic effectiveness along the tip for dirt purge flow at blowing levels of 0.10%, 0.19%, 0.29% and 0.38% core flow for a small tip gap (page 271).

Figure 7.17. Computational and experimental pitchwise-averaged adiabatic effectiveness along the tip for dirt purge flow at blowing levels of 0.10%, 0.19%, 0.29% and 0.38% core flow for a large tip gap (page 271).

Figure 7.18. Computational and experimental pitchwise-averaged adiabatic effectiveness along the tip for microcircuit flow at blowing levels of 0.5%, 1.0%, 1.5% and 2.0% core flow for a small tip gap (page 272).

Figure 7.19. Computational and experimental pitchwise-averaged adiabatic effectiveness along the tip for microcircuit flow at blowing levels of 0.5%, 1.0%, 1.5% and 2.0% core flow for a large tip gap (page 272).

Figure 7.20. Computational and experimental area-averaged adiabatic effectiveness along the tip plotted against dirt purge flow at various coolant blowing levels (page 273).

Figure 7.21. Computational and experimental area-averaged adiabatic effectiveness along the tip plotted against microcircuit flow at various coolant blowing levels (page 273).

Chapter 1

Introduction

As we enter the 21st century gas turbines continue to be an integral part of the world in which we live. Gas turbines provide the propulsive thrust to the airliners that transport us around the globe on a daily basis and to the aircraft of the United States Navy and Air Force. They power Army tanks, Navy ships and countless helicopters while providing power for many of the homes in which we live. Through continued research and innovation gas turbines will continue to offer more power and higher performance while operating more efficiently in today's environmentally conscious world.

The gas turbine engine traces its modern day roots to the early decades of the 20th century. On December 17, 1903 Wilbur and Orville Wright showed the world that human flight was possible. Their plane was powered by a homemade 4-cylinder, 12-horsepower internal combustion engine. At the time, the internal combustion engine was a logical choice to power aircraft, but these engines were limited, as their power-to-weight ratio was low. Initially, this was solved through engine turbochargers, but once again the planes were limited in size and speed. Realizing the potential of an engine that could potentially provide significantly more power and performance over the internal combustion engine, development began on aero gas turbines.

The inherent advantages of using turbine power were first realized when large-scale production of electricity began. Looking for ways to produce large amounts of power, both reliably and cost effectively hydro and steam turbines were used. These turbines had several advantages over other reciprocating engines such as the Otto and Diesel cycles. Reliability was generally higher because of a lack of rubbing and reciprocating parts, and the power output was higher when compared to an internal combustion engine of similar size.

The Brayton thermodynamic cycle defines the basic operation of a gas turbine and is shown in Figure 1.1. Air at atmospheric conditions is taken and compressed, after which fuel is added during a combustion process. The working fluid then travels to a

turbine where work is extracted before the gas returns to the atmosphere. In land-based applications the turbine normally provides enough power for the compressor with additional shaft power used for such purposes as creating electricity. For aero applications additional power beyond that needed to run the compressor is normally used for propulsion through either the momentum of exhaust gases or propeller shaft power.

The first gas turbines powering airplanes generally appeared as experimental fliers during World War II, as it was not until after the war that the gas turbine was fully adopted as the powerplant of choice for military aircraft. In 1939, the Germans launched the first jet-powered aircraft while the British followed suit in 1941, but these and subsequent engines were plagued by short lives, poor reliability and very high fuel consumption. During the 1950's the jet engine had become reliable and cost efficient enough to appear in commercial airliners.

The McDonnell XFH-1, commonly known as the Phantom, was one of the first jet powered aircraft in the United States military and is shown in Figure 1.2. Powered by a Westinghouse J30 turbojet engine this was the first jet airplane designed specifically for naval use. The plane first flew in January 1945 with a contract awarded in March for production of the aircraft. As World War II came to an end the need for the plane was significantly reduced and only 60 were manufactured, but this plane and engine were groundbreaking. In July 1946, with the help of a steam catapult the Phantom took off from the U.S.S. Franklin D. Roosevelt. At the time this was monumental as most jet powered aircraft required longer take-off distances and required more fuel than propeller aircraft. By 1948, the Phantom was part of the first all-jet squadron aboard a carrier on the U.S.S. Sappan. The overall range of the plane was limited due to the extremely inefficient engines giving it a range of just under 700 miles, but a cruising speed of 500 mph (225 m/s) was achieved, which was superior to anything in the Navy. As the jet engine quickly evolved during the 1950's the J30 powerplant was soon obsolete making the planes tour of duty relatively brief.

There are three basic types of aero gas turbine powerplants: turboprops, turbojets and turbofans. The turboprop design involves a gas turbine engine providing shaft power to a propeller as well as producing some thrust via the exhaust gases. The turbojet engine was the first to see significant testing and use in aircraft and is shown in Figure 1.3. It

achieves all of its propulsive forces through gases that pass through the engine. The turbine provides just enough shaft power for the compressor with the remaining energy used for propulsive forces. A derivative of the turbojet is the turbofan in which air is diverted around the main engine through bypass ducts creating additional thrust. Today, the turbofan and turboprop engines power nearly all commercial and military planes.

One plane receiving a great deal of press in recent years is the Joint Strike Fighter shown in Figure 1.4. This plane, designed by Lockheed Martin, was chosen over a rival aircraft presented by Boeing in 2001, and will be powered by the Pratt and Whitney F-135 turbofan engine, a derivative of the F-119 as seen Figure 1.5. Some of the technology being considered for use in the F-135 is explored in several studies presented in this thesis.

The gas turbine can be divided into three basic components consisting of a compressor, combustor and turbine as shown in Figure 1.3. The compressor serves to intake air at atmospheric conditions and compress it to levels near 30:1. The compressed air then travels to the combustor where fuel is added and ignited creating intense heat, and temperatures in excess of 3000° F for aero engines. Just downstream of the combustor is the turbine section, which is exposed to some of the hottest temperatures within the gas turbine. In an aero engine the turbine is responsible for extracting enough power to run the compressor, while land-based turbines extract as much power as possible for conversion to such things as electricity, through shaft power.

The focus of this research is based within the turbine section. With gas temperatures (3000° F / 1650° C) typically exceeding the melting point of the blade materials (2200° F / 1205° C) it is extremely important to effectively cool the blades to prevent failure. Cooler air (1250° F / 675° C) from the compressor is diverted around the combustor and serves to cool both the combustor lining and turbine section. Reducing temperatures within the turbine by a mere 50° F (28° C) can have far-reaching effects on the life and performance of a gas turbine by increasing blade life by a factor of two.

Cooling is accomplished through a number of methods that have evolved along with the gas turbine. Figure 1.6 shows a cross section of turbine vanes and blades along with three primary cooling methods. The first cooling method seen in turbine blades involved cooler air from the compressor being circulated throughout a hollow blade

cavity containing serpentine passages allowing for convective cooling. The serpentine passages evolved into impingement cooling techniques whereby the cooling air from the compressor would pass through many of the same serpentine passages, but be blown through high velocity jets onto internal hot spots. The high velocity jets resulted in a lower air temperature with relatively good localized cooling. Another cooling technique prevalent in most modern-day engines is the use of film cooling in which cool air from inside the blade is injected through the surface to provide a thermally cooler layer along the blade.

The tip region of a turbine blade, as shown in Figure 1.7, is one area in particular that experiences significant problems. To maintain the integrity of the tip section various cooling methods were studied as part of the work presented in this thesis. Figure 1.8a-c shows cooling from microcircuit channels with film cooling exhaust holes that was a primary focus of the tip work. Microcircuits are a new and untested approach to blade cooling. Currently, most blades are outfitted with internal serpentine passages that provide relatively good internal cooling, but the microcircuit may potentially offer turbine designers the ability to significantly increase blade cooling while using less cooling air, resulting in added blade life, durability, and engine efficiency. The operation of a microcircuit involves coolant gases traveling through a series of tiny cavities located near the blade surface to provide extensive internal cooling via conduction and convection heat transfer before exiting through a series of holes. Figure 1.8b shows the tip microcircuit with the air passages (colored blue) positioned over a large portion of the blade in order to maximize cooling. Once the cool gas has exhausted into the mainstream it provides film-cooling over the tip surface as the cooler air travels through the tip gap.

A detailed view of the tip leading edge is shown in Figure 1.8c. Important to notice is the small distance between the microcircuit ducts and tip of the blade, which could permit a great deal of heat to be conducted away from the hot tip. Along the tip there are a total of sixteen exhaust ducts that serve to provide film cooling over a substantial part of the blade tip. Considerable analysis was also spent studying the effect of tip leakage flows and dirt purge cooling holes. Dirt purge holes are shown in Figure 1.7 and in Figure 1.8a-c and are found in most blades as they are a necessary part of the blade casting process. In addition to their required presence during the manufacturing of

the blade, they also serve to exhaust dirt and debris within the engine in the hopes of preventing the more important microcircuit holes from becoming blocked as well as provide coolant over the leading edge.

A detailed computational study of a turbine blade with microcircuit and dirt purge cooling was performed to examine both flow and cooling characteristics when exposed to two different tip gap sizes and various blowing ratios. In addition to the combined microcircuit and dirt purge study, tip cooling was also examined with only exhaust from dirt purge holes. Computational results are discussed and compared to experimental measurements for benchmarking. In particular, the focus is on the effects of various tip gaps and blowing ratios on temperature levels along the blade tip and shroud.

Many of the same factors that affect tip performance are also prevalent around the base of the blade (Figure 1.7a). This area, referred to as the platform (or endwall), has a very large surface area and like the tip is exposed to high temperatures from the upstream combustor. The large platform area makes it very difficult to cool without the use of significant amounts of coolant. Reducing the amount of cooling air needed in the engine is very important to improving engine performance as it takes a great deal of work to compress atmospheric air and any air used to cool the engine cannot be used during the combustion process to make power. When manufactured, turbine blades are generally made as single parts with multiple blades being assembled to form a radial pattern. The interface of each blade platform is difficult to seal and thus coolant flow leaks out of this gap, also known as a gutter. Other areas where substantial leakage occurs are both upstream and downstream of the blade where the turbine platform meets the stator platforms. Termed front and aft rim leakage, respectively, the cooling effectiveness of these leakage flows are generally unknown, but are inherent to all engines. The use of leakage coolant with the addition of microcircuits with exhaust film cooling along the platform was examined as the focus of the second part of this study.

Computations with various platform leakage configurations and microcircuit film cooling slots were completed with a series of cooling rates in an attempt to maximize cooling while using the smallest amount of coolant. Similar to the tip studies, the computational data will have experimental data for benchmarking, but the data will not be completed in time for inclusion in this thesis.

Reducing the wear and tear on turbine vanes and blades is extremely important to increasing engine performance and efficiency, allowing engines to run hotter and longer. Figure 1.9a-c depicts three parts from a turbine. The first part shown in Figure 1.9a is a stator vane pulled from a high-pressure turbine after 4,000 flights and over 11,000 hours of service. Notice that the back part of the vane is missing and has broken off over the course of operation, while many of the film cooling holes located throughout the surface are clogged with dirt and debris. Cracks are also beginning to form throughout the surface. Figure 1.9b-c shows two turbine blades. The first has been pulled from a sand laden environment after 4,500 flights and over 8,200 hours of operation. This blade has performed well considering many of the film-cooling holes are partially or fully blocked by sand and other debris. The second blade (Figure 1.9c) is shown before entering an engine and does not yet have any film cooling holes.

A computational study provides valuable information about the flow and heat transfer phenomena that occur inside a gas turbine. In most cases, it is difficult if not impossible to take experimental measurements while the engine is operating, so that computations provide a great deal of information to engine designers. These computations also provide the ability to examine many different cooling schemes in a short time and at a reduced cost when compared to running experimental tests. When experimental results are available the computational data can be benchmarked to determine the validity, as was done for some of the cooling techniques studied with this research.

Chapter 2 of this thesis discusses some of the current literature that is available concerning tip and platform flows and cooling. In particular, emphasis is placed on past research performed with blowing along the tip and with work dealing with platform cooling via film cooling and leakage flows. It turns out that very little work has been done to explore either tip blowing or platform leakage flows, making the research presented in this thesis important to understanding many of these complicated phenomena. Detailed geometry and test matrices for the work presented in this thesis are presented in Chapter 3 while the computational methodology is presented in Chapter 4. Detailed results from the tip study are given in Chapter 5. Platform results are discussed in Chapter 6. A comprehensive benchmarking analysis is performed against

experimental data taken along the turbine tip in Chapter 7 while Chapter 8 summarizes the work and accomplishments.

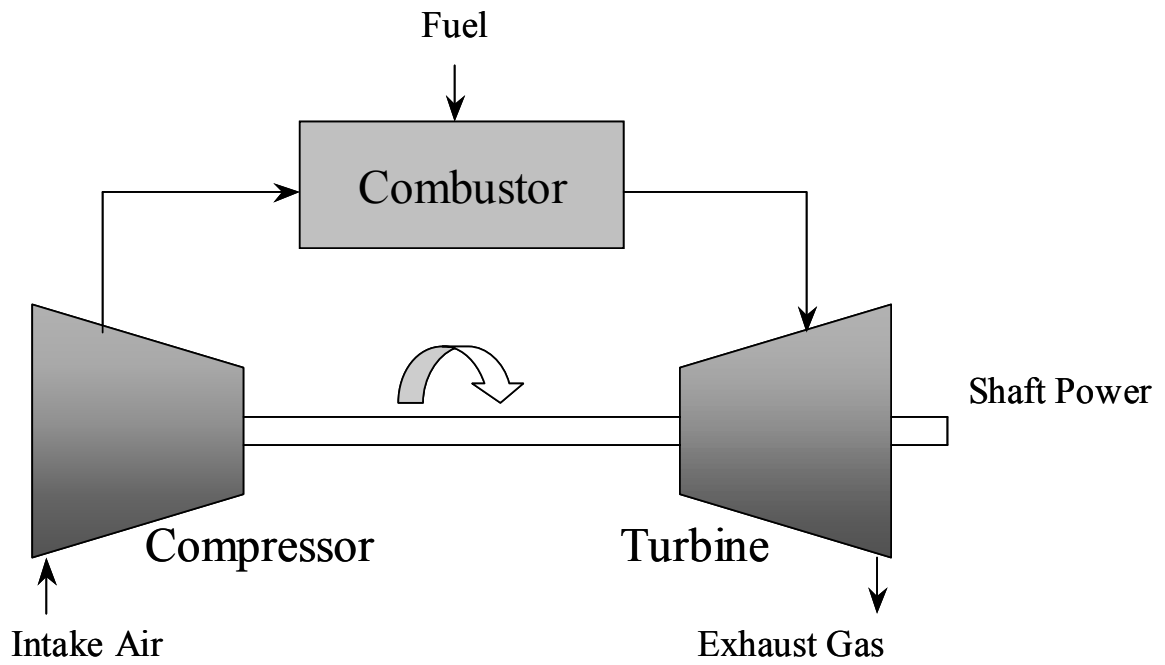


Figure 1.1. Diagram of the Brayton Cycle representing a gas turbine engine.



Figure 1.2. McDonnell XFH-1, Phantom, powered by the Westinghouse J30 turbojet engine. (courtesy www.mundoavion.com)

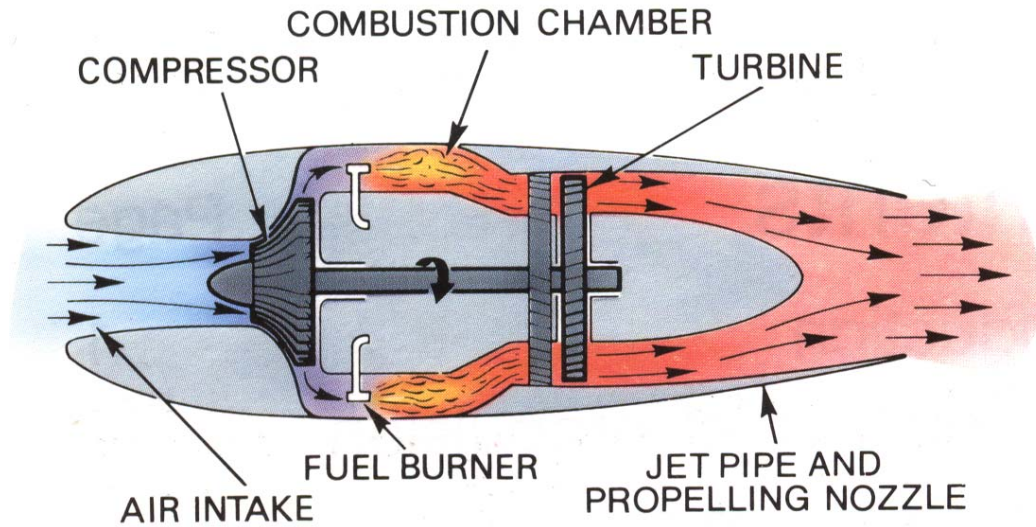


Figure 1.3. Schematic diagram of a turbojet engine showing the compressor, combustor and turbine sections. (courtesy Rolls-Royce, 1992)



Figure 1.4. Lockheed Martin X-35, Joint Strike Fighter, powered by the Pratt and Whitney F-135 turbofan engine, a derivative of the F-119 engine. (courtesy United States Air Force)

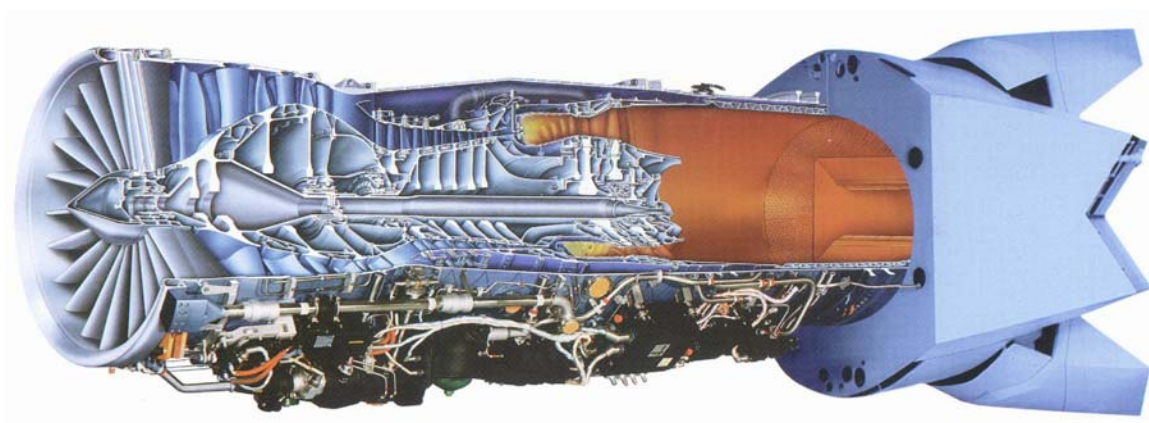


Figure 1.5. Pratt & Whitney's F-119 turbofan engine. (courtesy Pratt & Whitney)

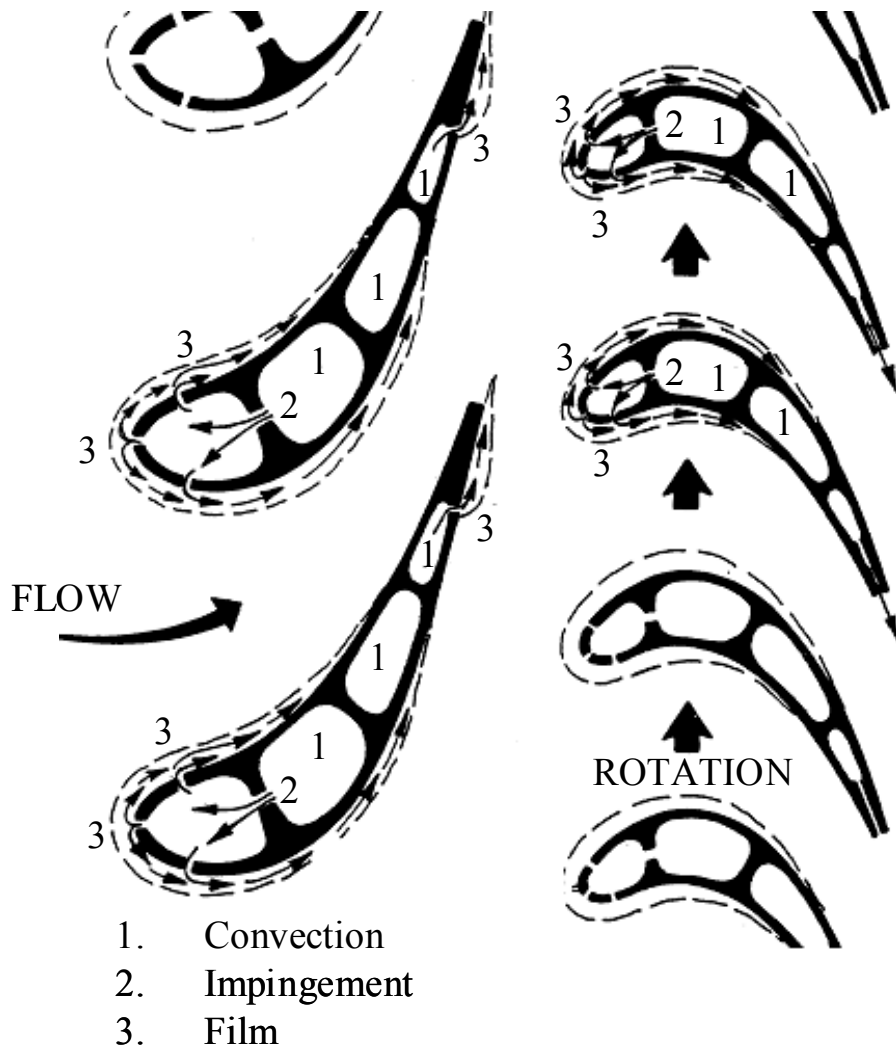


Figure 1.6. Various cooling methods used within a gas turbine including convective, impingement and film cooling. (courtesy General Electric Aircraft Engines)

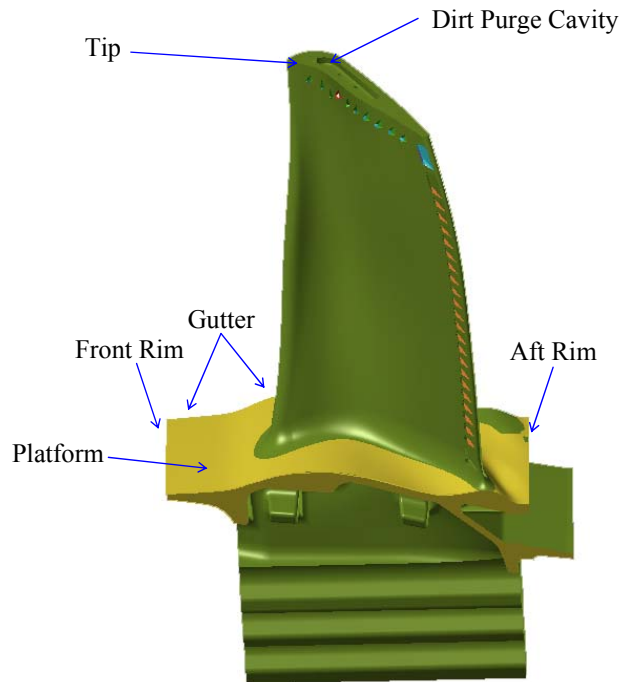


Figure 1.7. Diagram of a single turbine blade with the tip and platform highlighted as well as the dirt purge and various platform leakage locations. (courtesy Pratt & Whitney)

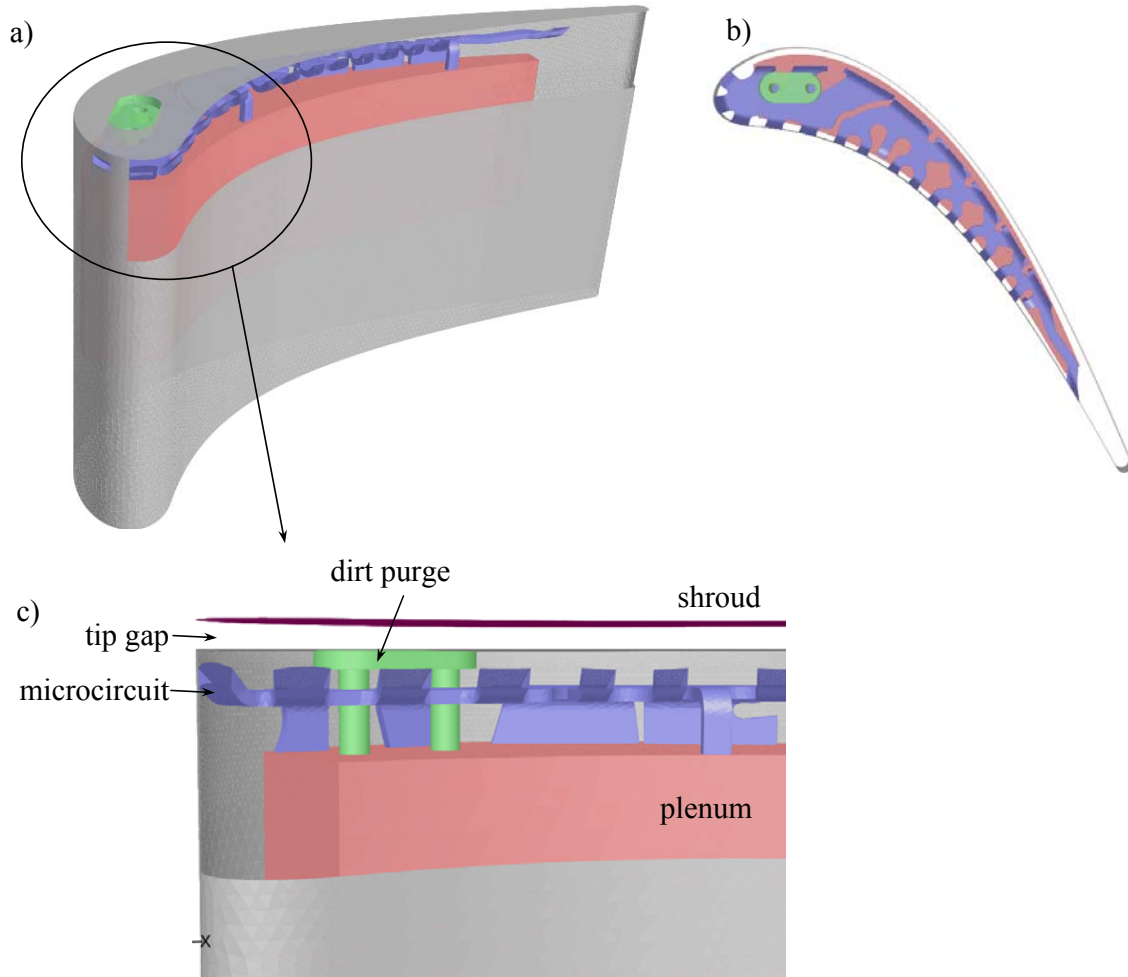


Figure 1.8a-c. Diagram of a) microcircuit embedded within the blade with part of the blade sheathing removed, b) top view of the blade with the tip sheathing removed showing the microcircuit extending over a large portion of the blade, and c) enlarged view of leading edge region showing the tip gap, shroud, microcircuit and other relevant geometry.

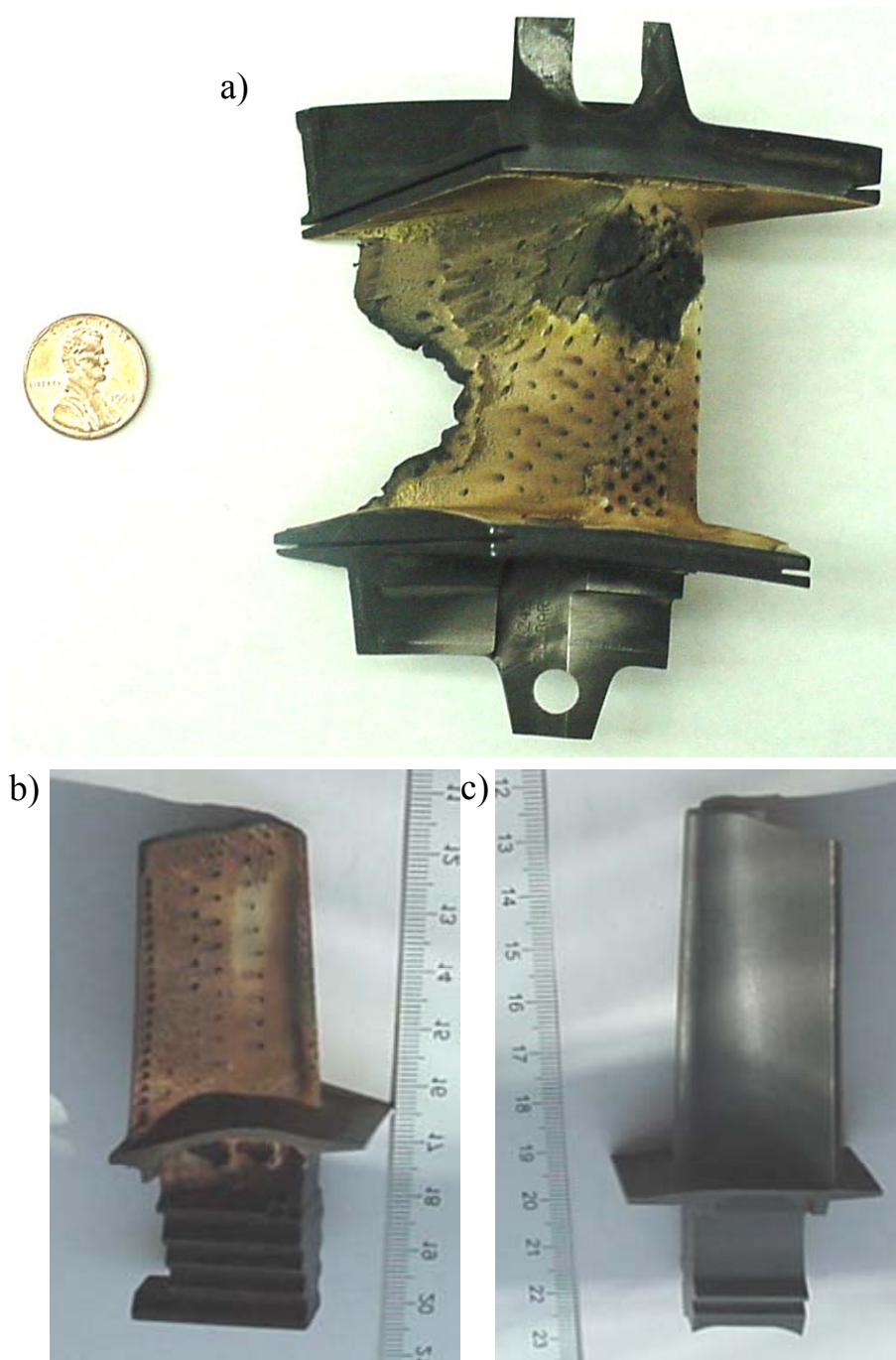


Figure 1.9a-c. Two turbine blades and one vane: a) turbine stator vane after being removed from an engine with 4,000 flights and 11,000 hours of operation, b) turbine rotor blade after operating in a sand laden environment for 8,200 hours and 4,500 flights, and c) turbine rotor blade before entering an engine and without film cooling holes.

Chapter 2

Literature Review

The gas turbine has been the focus of considerable research during the last century as designers strive to build better engines. Much of what goes on inside an engine is not well understood since experimental work is very challenging and expensive. This means that new technologies are slow to reach the market with development times for some technologies taking a decade or more. As greater efficiencies and more power from the engine are desired it becomes even more important to gain a better understanding of the physics involved inside the engine. This increased understanding of flow and heat transfer phenomena will be discussed in the following chapter with specific interest given to past work dealing with turbine tips and platform studies.

Numerous studies since the advent of the modern gas turbine have addressed the tip region of a turbine blade, but most work has focused on increasing turbine efficiencies through the reduction of aerodynamic losses. Only recently has work begun to investigate heat transfer effects along the tip with only a handful researchers studying the effects of coolant gases being released in the tip region. The tip region is subjected to extremely severe conditions with many factors making the blade tip a very complex area of study. Some of the problems faced by blade designers include the tip being subjected to some of the highest transfer within the turbine that creates large temperature gradients. Another cause of substantial temperature gradients is the unsteady gas temperatures from the upstream combustor. These two phenomena may result in severe thermal and mechanical stresses. High stresses lead to cracking which could cause a loss of material with the loss of material ultimately leading to adverse effects on the thermal and flow fields. Other complexities include the addition of film cooling and oxidation to name a few [Bunker, 2000a].

In the past, considerable resources have been spent focusing on the reduction of leakage flow moving across the tip, as this leakage has a substantial effect on the overall turbine efficiency. The leakage that occurs across the tip gap from the pressure to suction side is inherent to the blade and is a function of the blade loading. A second important

factor dictating tip leakage is the distance between the blade tip and the outer shroud. Because this gap is relatively small, viscous forces in the gap are important. One important flow feature that has been identified by past investigations is a tip leakage vortex. The vortex results from a velocity differential between the flow of the mainstream gas and the tip leakage flow as it exits along the suction side of the gap. Another important flow feature, which has not only been identified by computational fluid dynamics (CFD) studies, but also heat transfer studies, is the presence of a flow separation zone along the pressure side of the blade tip as flow enters the gap. An overview of some past tip studies will be presented in Section 2.1 to familiarize the reader with some of the important findings presented in published literature and provide the reader an understanding of what lies ahead with the research presented in this thesis.

The platform region of a turbine, like the tip, is exposed to very demanding conditions. This area is generally cooled through a combination of film-cooling holes and leakage flows. The leakage air comes from a variety of sources including the gap between two adjacent turbine platforms, referred to as the gutter, as well gaps located both upstream and downstream of the turbine blades, which are required to accommodate the rotating blades. For the most part, the effects of leakage flows along the platform are unknown as there is very little in the literature discussing the potential benefit of this cooling. Section 2.2 provides a general overview of turbine platform cooling with particular attention paid to both film cooling and leakage flow studies.

2.1 Tip Studies

The rigorous demands of a real-life engine make it extremely difficult, costly and sometimes impossible to run experimental tests to examine the phenomena that occur within the engine. For this reason it is very helpful to perform experimental tests and simulations by removing parts from the gas turbine in order to obtain more information about specific flow and heat transfer features. This study, for example, looked at over twenty different tip configurations in a matter of months that if studied within an operational engine would have not only lasted considerably longer, but would have been

very expensive. Of course when moving from a gas turbine to various experimental rigs there is certainly not a one to one relationship for some test parameters, but nonetheless a great deal of information can be obtained quickly and cost effectively when compared to alternative methods.

The computational and experimental [Couch, 2002] work of this study was performed on a stationary, linear turbine cascade, meaning several two-dimensional turbine blade models were positioned to match many of the geometric features within a true turbine arrangement. Several of the differences between this study and a gas turbine include a linear cascade as opposed to a radial arrangement and the lack of rotation. Upon hearing that there is no relative motion between the blades and outer casing one may begin to wonder about the legitimacy of this type of test, but in fact work by many researchers have concluded that rotational effects have little effect the flow within a turbine cascade. In an investigation of tip gap flows undertaken by Morphis and Bindon [1988] they specifically discuss the effect of relative motion on the blade tip pressure distribution with one of their primary conclusions being that relative motion of the outer shroud had little effect on the blade tip pressure distribution. They also found that the shroud motion had little effect the tip gap flow.

Tallman and Lakshminarayana, [2001a] explored variations in the flow field using a rotating rig as opposed to a static turbine cascade. Rotational features that are not considered in a stationary test rig include centrifugal forces, the Coriolis forces and inlet rotational effects. He found that qualitatively, the behavior of the tip leakage vortex in the turbine rotor is very similar to that observed in a static cascade with the aerodynamic losses also being very similar.

A comprehensive summary of both heat transfer and flow phenomena is discussed by Bunker [2000a]. The study of blade tip heat transfer has only been under investigation for the last several decades with tip flows having been investigated for considerably longer. Several flow features and characteristics have been found to exist around the tip and are highlighted by Bunker in Figure 2.1a-c. One of the most significant flow features to take note of is the development of a tip leakage vortex. This vortex results from flow traveling through the tip gap, creating substantial losses within the turbine. As the flow leaves the tip gap, it re-enters the mainstream flow at a different direction and magnitude

than the mainstream flow creating the vortex. Some of the first work focusing on flow through a turbine was conducted by Allen and Kofskey [1955] in which they looked at secondary flows through smoke visualization. In the decades following the work of Allen and Kofskey extensive flow studies were examined by many researchers.

Recent tip gap flow studies have been performed by Morphis and Bindon [1988]. In addition to discussing the effects of relative motion between the blade and shroud they also studied blade edge radius, and gap size on the blade tip pressure distribution. After concluding that relative motion of the outer shroud had little effect on the blade tip pressure distribution, nor did the shroud motion effect the tip gap flow, they provided a detailed discussion of the flow separation zone along the blade tip. Additional work presented by Bindon [1989] quantifies the losses associated within the tip. Loss contributions from such things as mixing, internal gap shear flow and wall/secondary flows were quantified. Mixing losses were defined as the losses that occur when the tip leakage vortex and other smaller vortices mix with the mainstream flow. Wall/secondary losses were considered to be the result of skin friction shear stress on the fluid flow as it moves across the walls while internal gap shear occurred by frictional losses within the gap. It was determined that 13% of losses were associated with endwall/secondary flow while 48% and 39% were due to mixing and internal gap shear flow, respectively. Also important to note was the substantial increases in turbine efficiencies that resulted by a reduction in the size of the tip gap.

A computational study by Tallman and Lakshminarayana [2001b] discusses tip leakage phenomena in turbines using a computational, pressure-correction based, three dimensional Navier-Stokes code. Their results showed that a reduced tip clearance results in less mass flow through the gap, a smaller leakage vortex, and less aero losses in the tip gap. Tallman and Lakshminarayana [2001a] performed another computational tip study to look at the effects of various blade chamfers on the effect of flow through the tip gap region. They concluded that chamfering of the blade tip near the leading edge of the gap and across the entire gap failed to reduce the size and strength of the leakage vortex. However, by chamfering the blade tip near the trailing edge of the gap, a decrease in both size and strength of the tip leakage vortex occurred.

Heat Transfer & Squealer Tips

Some of the earliest work performed to measure heat transfer along a blade tip was undertaken by Mayle and Metzger [1982]. Average heat transfer coefficients were measured for nominally flat tip passages, simulating a blade tip, with various Reynolds numbers and rotational speeds. More recent heat transfer measurements along the blade tip have been made by several researchers including Bunker, et al. [2000] and Papa, et al. [2002] while Azad, et al. [2000a and 2000b] has made computational predictions. These researchers have pinpointed several regions that exhibit distinct characteristics along the blade tip region. One region, located in the thickest part of the blade, near the leading edge, has been shown to have low convective heat transfer coefficients as a result of low convective velocities. In contrast, two regions having the highest heat transfer coefficients were the leading edge region and along the pressure side of the blade where a flow separation region was present. The general consensus among these papers was that with a larger tip gap, overall heat transfer coefficients increase due to the larger leakage flows.

A method commonly used to reduce leakage flow within the tip gap is to use a squealer-tip, which acts as an air seal by increasing the flow resistance. Figure 2.1b illustrates a cross-sectional view of the squealer tip. Computational predictions by Azad [2000b] concluded that the addition of a squealer tip served to decrease heat transfer along the mid-chord by 25%, but there was a 25% increase in the leading edge heat transfer since the leakage flows had only been redistributed.

Bunker and Bailey [2000] have also studied the effect of squealer cavity depth on turbine blade heat transfer and concluded that the general rule of a deeper squealer cavity resulting in lower heat transfer coefficients held true for their work. Overall heat loads were about 10% lower when compared to a flat tip model with one particular geometry having a tip gap to squealer gap depth ratio of 2. Heat transfer was reduced by as much as 50% for the deepest squealer tip with a tip gap to squealer gap depth ratio of 0.7.

Azad, et al [2000a and 2000b] studied heat transfer along flat and squealer tips. Looking at various tip gap heights of 1%, 1.5% and 2.5% of the blade span and turbulence intensity levels of 6.1% and 9.7%. He concluded that the squealer geometry provides a lower overall heat transfer coefficient when compared to the flat tip blade. In

addition, his results showed no variations in heat transfer within the tip gap for the two turbulence levels examined of the study.

Computational work by Yang, et al. [2002] to study tip heat transfer looked at three different turbulence models of increasing complexity: standard k- ϵ model, RNG k- ϵ model and Reynolds-Stress model along a flat blade tip. In particular, the researchers were focused on heat transfer predictions for which they obtained satisfactory agreement to experimental data from Azad [2000a] using all three turbulence modeling packages. In fact, there was no significant improvement in results when using the more complex Reynolds-Stress model when compared to k- ϵ and RNG k- ϵ models.

Ameri and Bunker [2000] presented a computational study of tip heat transfer with a comparison to experimental work by Bunker et al [2000]. The study examined two different flat tip geometries with the only difference being one tip had a sharp edge while the other tip was rounded as shown in Figure 2.2a-b. Using the k- ω turbulence model, the code showed better agreement for the rounded edge rather than the sharp tip case. There was speculation by the researchers that the agreement with the rounded tip was superior to that of the sharp edged tip because the computational model could not provide an accurate prediction of the flow separation zone, which was not present along the rounded tip.

Tip Blowing

One method for reducing the leakage flow while also improving the thermal environment along the blade tip is to inject coolant in the tip region. Bunker [2000a] states that to date, there has been very little fundamental blade tip film cooling research reported in the literature even though film cooling is widely used along the tip from such things as dirt purge holes and pressure side film cooling holes. Table 2.1 shows all of the previous studies available in open literature involving blowing from a tip, which to the knowledge of this author includes the work of Kim and Metzger [1995], Kim, et al. [1995], Kwak and Han [2002a, 2002b], and Acharya, et al. [2002].

Prasad [1999] studied the effect of tip blowing on turbine aerodynamic efficiencies for various turbine blades. His results indicated that an optimum tip blowing mass flow rate corresponding to 0.5% of the turbine inlet mass flow rate equates to an

increase in turbine efficiency of about 0.8%. Another aspect of the study examined the unsteady flow field along the outer shroud, which in some instances erode due to high heat loads. Unsteady pressure measurements along the shroud indicated the existence of a separation bubble on the blade tip, causing a vena contracta to form in the blade tip. The vena contracta was determined to be a function of blade tip clearance for a smooth tip with no correlation found for rough blade tips. The pressure measurements suggested that the shroud was typically exposed to steady flows while the only unsteady flows were found within the tip gap. Prasad also states that tip blowing tends to alter the pressure signature of the tip leakage flow along the shroud.

Yang, et al. [2002] reported computational studies using the same code and methods used for the work to be presented in this thesis to directly compare with the experimental heat transfer data given by Azad, et al. [2000a, 2000b]. In particular, Yang was able to compare his computational work to heat transfer and pressure measurements along a tip, but there was no blowing data for benchmarking. He found reasonable agreement between the experiments and computations.

After looking at heat transfer coefficients the researchers also simulated coolant blowing from the tip. Testing three different gap heights of 1%, 1.5% and 2.5% of the blade span Acharya, et al. [2002] found that film coolant injection lowered the local pressure ratio and altered the nature of the leakage vortex. In Figure 2.3a-c film cooling effectiveness contours are plotted for three tip gap sizes. Important to notice with these contour plots are the blue regions corresponding to low effectiveness (hot) and red regions corresponding to high effectiveness (cold), which differs from the format in which data is presented in this thesis. High film cooling effectiveness and low heat transfer coefficients (not shown in the figure) are obtained along the coolant trajectory with the lateral spreading of the coolant jets being quite small for all cases. With an increasing tip gap the coolant was able to provide better downstream effectiveness through increased mixing. Figure 2.4a-c shows the effect of the tip gap height on film cooling effectiveness along the shroud. At the lower tip gaps, the coolant was shown to impinge directly on the surface of the shroud, leading to high film effectiveness at the impingement point. As the gap size increased, the coolant jets were unable to penetrate all the way to the shroud and the cooling dropped dramatically.

Streamlines and velocity magnitude contours in a plane near the mid-chord are shown in Figure 2.5a-b for two blowing ratios ($M=0.5$ and $M=1.5$). At the lower blowing ratio, the coolant did not penetrate all the way to the shroud, and the leakage from the pressure side to the suction side of the blade was not deflected by the coolant jet. As the blowing ratio was increased to $M=1.5$, the coolant jet penetrated all the way to the shroud.

Figure 2.6a-c shows the film cooling effectiveness on a squealer tip for three different tip gap heights of 1%, 1.5% and 2.5% blade span. Comparing these results to those seen for a flat tip in Figure 2.3a-c one can see that there are some substantial differences. Instead of the high effectiveness region being downstream of the cooling holes as seen with a flat tip, the high effectiveness region was confined to the vicinity of the coolant holes along the pressure side with the flow controlled by complex three-dimensional patterns inside the squealer cavity. Acharaya suggested relocating the cooling holes from the pressure side to a more central location between the pressure and suction sides of the blade may result in better cooling. As the tip gap increased the cooling effectiveness in most of the cavity diminished while the area in the direct path of the coolant experienced improved effectiveness.

Kim, et al. [1995] presents a summary of the experimental work that Metzger performed on tip blowing. In addition to concluding that there is only a weak effect of the relative motion between the blade and shroud on tip heat transfer coefficient he stated that there is a strong dependency of tip film-cooling on the shape of the hole and injection locations. Four tip blowing configurations were explored in the study of interest with the geometries shown in Figure 2.7a-d. The geometric configurations consisted of (1) discrete slots located along the blade tip, (2) round holes located along the blade tip, (3) angled slots positioned along the pressure side and (4) round holes located within the cavity of a squealer tip. These blowing configurations were tested with tip gaps having a blade thickness to tip gap height ratios of 9.1 and 15.2, respectively. Three Reynolds numbers of 15×10^3 , 30×10^3 and 45×10^3 based on upstream velocity and hydraulic diameter were examined with cooling rates set to provide values of film-to-mainstream mass flow ratios ranging from 0.016 to 0.223.

Figure 2.8a-d shows some effectiveness results taken for each of the four geometries displayed in Figure 2.7a-d. In Figure 2.8a effectiveness measurements were taken with a discrete slot and the results were very promising. Spanwise distance in the figures is plotted along the x-axis while effectiveness is plotted along the y-axis with results presented at various locations downstream of the injection points. Cooling levels just downstream of the slots varied from 1 to levels near 0.65 with cooling further downstream smoothed out considerably and varying between 0.35 and 0.5. At the furthest downstream location cooling levels dropped to just below 0.2. Comparing the discrete slots to the holes of Figure 2.8b, Kim saw a substantial decrease in cooling effectiveness at the same downstream locations. The cooling fluid did not cool nearly as well when injected from holes, but the large gradients that were seen with slot cooling were no longer present for the hole geometry. Maximum effectiveness from the holes reached levels around 0.4 and dropped to 0.1 at the most downstream locations. The pressure side holes of Figure 2.8c provided cooling levels of similar magnitude to the tip holes with some added spanwise variation. Cooling levels varied from 0.3 to 0.5 at the most upstream location and from 0.1 to 0.2 at the downstream location. Finally, the grooved tip geometry exhibited relatively poor cooling when compared to the others, but the squealer tip in general was not subjected to the same fluid flow phenomenon as the flat tip cases. Kim also reports that an increase in coolant mass flow generally yields improved cooling, but this was not necessarily true for pressure side injection.

In another study Kim and Metzger [1995] examined cooling effectiveness for the geometry shown in Figure 2.9a-b. These cooling slots were located at the edge of the pressure side and measured 0.318cm in width and 0.953cm in length. Two different tip gap heights (with a tip gap height to injection hole width ratio of 1.5 and 2.5) and three Reynolds numbers (15×10^3 , 30×10^3 and 45×10^3 based on inlet velocity and hydraulic diameter) were examined. They concluded that film cooling along the pressure side corner of the blade tip can provide significant protection of the tip from convective heat transfer of the hot leakage gases.

Figure 2.10a shows a typical effectiveness distribution at various locations downstream of the film cooling slots with a small tip gap, blowing ratio of $M=0.3$ and Reynolds number of 30×10^3 . Just downstream of the slots cooling levels varied from 1,

in the direct path of the coolant to values just above 0.5 in the areas between cooling slots. The large thermal gradients started to degrade as the coolant mixes with hot mainstream gases before reaching levels of 0.15 at the furthest downstream position. In Figure 2.10b span-wise averaged effectiveness was plotted for the three Reynolds numbers of interest with a blowing ratio of $M=0.5$ and a large tip gap. The curves show that effectiveness did not appear to vary much with the mainstream Reynolds number, but instead varied considerably with the blowing ratio.

Span-wise averaged effectiveness was plotted in Figure 2.11a-c for various blowing ratios and Reynolds numbers. Figure 2.11a depicts averaged effectiveness at four blowing ratios and a mainstream $Re=15 \times 10^3$. Increased effectiveness was seen as the blowing ratio increases from 0.1 to 0.9. This trend continued for the two larger Reynolds numbers of 30×10^3 and 45×10^3 that are displayed in Figures 2.11b and c, respectively.

Using hue detection based transient liquid crystal technique to measure heat transfer coefficients and film-cooling effectiveness Kwak and Han [2002a, 2002b] reported measurements for tip gaps measuring 1%, 1.5% and 2.5% of the blade span with averaged blowing ratios of 0.5, 1 and 2. Cooling holes were placed along the pressure surface at a 30° breakout angle and on the tip surface at a 90° angle for a flat and squealer tip geometry as shown in Figure 2.12a-b.

Figures 2.13a-c and 2.14a-c show effectiveness measurements along a flat turbine blade tip (Kwak and Han, 2002a). In Figure 2.13a-c coolant was released from only the tip cooling holes with a constant tip gap height of 1.5% of the total span and three blowing ratios ($M = 0.5, 1, 2$). Because of the 90° injection angle the coolant flow seemed to mix out with the leakage flow resulting in low effectiveness. At all blowing ratios the maximum effectiveness was 0.2 and was seen just downstream of the cooling holes, but with additional cooling flow the effectiveness did improve. Figure 2.14a-c shows coolant being released from pressure side and tip cooling holes. As with the tip cooling cases, there was increased cooling effectiveness with additional mass flow. The highest effectiveness was seen along the trailing edge, which results from the accumulation of film cooling air exiting the pressure side holes. It is also worth noting that pressure side injection at a blowing level of $M=0.5$ was not present along the tip.

Only at levels of $M=1$ and to a greater extent $M=2$ did the pressure side cooling holes provide significant film cooling effectiveness.

In another study by Kwak and Han [2002b] cooling effectiveness along a squealer tip was presented. Figures 2.15a-b and 2.16a-b present cases that are similar to those with a flat tip (Figure 2.13a-c and 2.14a-c) with the only variation between the cases being the tip geometry configuration. The tip gap height (1.5% span, where gap height is defined by the tip height rather than the squealer height) and blowing ratios remain the same. Comparing the flat tip cases of Figure 2.13a-c to the squealer cases of Figure 2.15a-b showed a substantial improvement in effectiveness with the addition of a squealer tip. The cooling gases circulate within the squealer tip providing a better distribution of the coolant along much of the tip compared with no squealer cases. Only along parts of the suction side was the cooling effectiveness poor. As seen with a flat tip, the trailing edge exhibits good cooling due to the accumulation of coolant that exits in this area. More coolant results in improved effectiveness.

Figure 2.16a-b show a squealer tip with coolant released from pressure side and tip holes. Results show coolant injected from the tip holes was pushed toward the pressure side and exits the cavity near the trailing edge. Pressure side coolant was carried over the pressure side rim, increasing effectiveness along the rim while some of the coolant was reported to travel directly to the suction side rim. In general, the researchers concluded that film cooling effectiveness increased as blowing ratio increased for all cases. When comparing cases with just tip coolant injection (Figure 2.15a-b) to cases with tip and pressure side coolant (Figure 2.16a-b) it was determined that the pressure side injection was beneficial due to its ability to carry coolant over the blade as well as act as a flow resistance for the tip leakage flow. They also determined that high film cooling effectiveness appeared near the trailing edge of the cavity due to coolant accumulation.

In summary, there are only a handful of studies that have addressed blowing in the tip gap region. Much of the current work in the literature has focused on turbine tip flows in an attempt to reduce aerodynamic losses that are associated with this region, while more recent work has been aimed to both measure and predict heat transfer characteristics along flat tips. While squealer tips are somewhat relevant to the work

presented in this thesis, being of similar depth to that of a dirt purge cavity, there are still substantial differences due to the size of the cavity being much larger in extent for the squealer tips. None of these past studies have addressed a realistic aero-engine design that contains the presence of the dirt purge geometry with blowing nor do they exhibit extensive pressure side blowing from microcircuit channels with film cooling hole exits. For that reason, the work presented in this thesis relating to tip cooling is unique to the literature in the field.

2.2 Platform Studies

Platform studies have been the focus of numerous research projects for the last quarter century. During this time considerable information concerning flow and heat transfer phenomena within the turbine has been gained, but considerable work still remains. The turbine platform, (also known as an endwall) is found in both stationary vanes and rotating blades. As flow exits the combustor at extremely hot temperatures it first encounters the turbine stator vanes that serve to direct the flow toward the downstream rotating blades. Work is then extracted from the fluid as the blades rotate with the fluid exiting the first stage turbine. Some of the hottest gases in the turbine are seen just downstream of the combustor in the turbine vanes. For this reason considerable time has been spent studying the vane endwall. In fact, considerably less work has been performed on the region just downstream of the vane, namely the blade endwall. This section will serve to present some of the work performed on turbine vane endwalls in addition to much of the current work available on blade platforms.

Early endwall studies focused on examining the secondary flowfield. Work by Eckerle and Langston [1987] discusses the formation of a symmetric horseshoe vortices in front of a vane endwall junction and is as shown in Figure 2.17a. This vortex forms as the boundary layer along the platform begins to slow and stagnate as it approaches the airfoil. Pressure gradients near the endwall are present such that the flow separates and causes the boundary layer to roll-up creating a horseshoe vortex which splits into a

pressure side passage vortex and a suction side corner vortex. The passage vortex dominates the flow and results in significant aerodynamic losses, unwanted increases in heat transfer rates, and a reduction in film-cooling effectiveness. The effectiveness typically decreases due to the turbulent mixing from the vortex that in many cases pulls cooling away from the endwall and mixes it with hot mainstream gases. Additional models of flow through the turbine blade have been presented by Sharma and Butler [1987] and Goldstein [1988] in which more complex flow phenomena are presented. These models are shown in Figure 2.17b and c, respectively. The model by Sharma and Butler demonstrates the suction leg of the horseshoe vortex wrapping itself around the passage vortex instead of adhering to the suction side while the model by Goldstein is based on mass transfer results in which he proposes that the suction leg of the horseshoe vortex stays above the passage vortex and travels with it. In all three models there is some discrepancy in the location of the suction leg of the horseshoe vortex.

Turbine Vanes

Cooling effectiveness and heat transfer measurements along turbine platforms have been made by several researchers with much of the work focusing on the first stage turbine vane and the turbine-combustor junction. Some of the first work to address endwall cooling effectiveness was undertaken by Blair [1974]. In his study a flush slot with coolant injection was placed upstream of curved walls meant to represent nozzle guide vanes. Blair examined three different coolant mass flow rates which exhibited slight increases in effectiveness as the blowing was increased.

Endwall surface film cooling effectiveness was measured on a turbine vane endwall by Zhang and Jaiswal [2001] for holes placed upstream of the vane. Using a cooling mass of 0.5% to 3.0% of the mainstream gas flow they examined a double staggered row of holes and single row of discrete slots. Results indicated that film effectiveness increased non-linearly with the mass flow rate, indicating a strong interference between the cooling jets and endwall secondary flows. At low blowing rates they stated that the secondary flows dominated the near wall, resulting in low effectiveness, while higher blowing ratios showed the coolant momentum dominating the near wall flow and providing substantial cooling improvements.

Oke, et al. [2000] examined vane endwall cooling with the use of film cooling holes located upstream of an airfoil cascade. The cascade consisted of two passages in which he examined cooling patterns along a contoured endwall as shown in Figure 2.18. The cooling holes were oriented to achieve a 45° break-out angle with flowrates between 1.5% to 3.0% of the core flow used for cooling. Using staggered, discrete holes it was found that at a lower coolant flow rate (1.5% core flow) through the cascade the coolant flow was drawn across the endwall towards the suction side of the vane by cross-flow, while an increase in mass flow (3.0% core flow) caused a sufficient increase in the coolant momentum so that no migration is seen.

In a related study, the effects of a slot located upstream of turbine vanes is presented by Burd, et al. [2000a, 2000b]. The slot location is depicted in Figure 2.19 with bleed air fed through an inclined slot. The slot was discontinuous in the pitchwise direction with a break between the vanes and a 45° break-out angle into the mainstream flow. Using coolant ratios as high as 6% of the core flow, adiabatic effectiveness and heat transfer coefficients were recorded along the endwall as well as flow field measurements throughout the cascade. The coolant was found to provide very good thermal protection over most of the endwall as well as portions of the pressure and suction sides of the airfoil, but these results were only achieved when the slot flow (3.2% of mainstream flow) was strong enough to overcome the influence of near wall secondary flows. From a flow standpoint the combustor bleed cooling flow was found to impose no aerodynamic penalty, which is atypical of schemes where coolant is introduced within the passage for endwall cooling. This cooling scheme was also found to reduce secondary flow effects for the high cooling flows.

An experimental study by Colban and Thole [2003] examined effectiveness measurements along the endwall of a first stage turbine vane. Varying the combustor liner film-cooling and junction slot flows, (shown in Figure 2.20a-b) adiabatic effectiveness measurements were made for several cases. The results showed that varying the coolant injection from the upstream combustor liner leads to differing total pressure profiles entering the passage, while adiabatic effectiveness measurements do not show a uniform slot flow. Instead, coolant accumulates along the suction side of the vane and endwall. Increasing the slot cooling continued to reduce endwall temperatures,

which was not always true with upstream film-cooling. In a follow-up to the endwall effectiveness measurements Colban, et al. [2003] also examined flow and thermal field planes within the turbine vane cascade. In particular, the effects of additional slot flow on the development of secondary flows were discussed. Slot ingestion had been predicted in computational work by Stitzel [2001] (Figure 2.21) and was also measured for experimental cases, which resulted in a higher coolant temperature and decreased effectiveness. In addition, much of the coolant was pulled away from the endwall by secondary flows.

Turbine Blades

While there are many similarities between turbine vane and blade endwalls there are also notable differences. Two such variations include: flow entering turbine vanes is typically normal to the airfoil while blades have flow entering from an angle (as directed by the upstream vanes), and the geometry of the airfoils can vary substantially. Vane are normally designed to turn the flow such that the turbine blade can extract the most possible work from the fluid, meaning the turbine blade typically has a much greater angle of attack than a vane. One researcher to perform numerous blade endwall studies is R. J. Goldstein. Goldstein and Spores [1988] used a mass transfer technique to obtain a much greater detail of the convective coefficient than what can be obtained using discrete thermocouple measurements. Using mass transfer it was possible to correlate convection patterns with secondary flows. Their study helped to confirm the existence of several flow features in a turbine blade cascade including: corner vortices at the pressure side – endwall junction, a pair of vortices at the suction side – endwall junction, and leading edge corner vortices.

In related work to that of Goldstein and Spores, Jabbari and Goldstein [1993] provided a color visualization technique over the endwall and suction side of a turbine blade in which their results were supported by the earlier mass transfer studies of Goldstein and Spores.

In another study, Goldstein, et al. [1995] used a stationary turbine blade cascade to measure convective transport and study secondary flows. A wire is used to trip the boundary layer near the leading edge of the blade. The disturbance caused by tripping

the boundary layer created high mass transfer rate on the pressure side of the blade and in the laminar flow region along the suction side, but lowered the transfer rate along the turbulent portion of the suction side. The impact of vortices initiated near the endwall at the laminar to turbulent transition extend three-dimensional effects to approximately 0.8 chord lengths on the suction side and 0.2 chord lengths on the pressure side. The effect of the passage vortex and a new vortex induced by the passage vortex on the mass transfer was clearly evident along the suction surface of the blade. The influences of small, but intense corner vortices and the passage vortex on mass transfer were also observed along both the pressure and suction sides.

Wang, et al. [1997] used smoke ring wires and laser lights to study secondary flows along the endwall of turbine blades in a cascade. Figure 2.22a-b highlights the test facility and the blade geometry under consideration. Important to notice are the staggered blades, which are necessary to reproduce the flow angles seen with a blade geometry and the location of the smoke release (just upstream of the blades). During the experiments, researchers observed a periodically fluctuating horseshoe vortex system with a varying number of vortices near the leading edge of the cascade. Interactions between the suction side leg of the vortex of the horseshoe vortex and the passage vortex were also observed. A vortex not seen in previous work was shown to emerge about one quarter of the surface distance along the suction side of the blade. It was determined that this vortex was created by the passage vortex. Its path remains close to the suction surface and just above the passage vortex in a laminar flow region. From this study the researchers presented a modified flow visualization model for flow in a turbine cascade which is seen in Figure 2.23.

Computational work by Hermanson et al. [2003] resulted in the benchmarking of three computational turbulence modeling packages by examining their ability to adequately model heat transfer distributions along vane and blade endwalls. The modeling packages consisted of the $k-\epsilon$ realizable with wall functions, $k-\epsilon$ realizable with two layer zonal model and the V2F model, with computational results benchmarked against experimental data obtained by Cho, et al. [2001] from a scaled-up, low-speed test rig. Figure 2.24a-b shows experimental and numerical heat transfer results along the blade endwall. Quantitatively, the values are slightly underpredicted with the most

obvious regions being around the leading edge and downstream of the trailing edge. Results showed that all models accurately captured the secondary flowfield, but $k-\epsilon$ models did not perform well in predicting heat transfer measurements because of a lack of near wall turbulence modeling capabilities. Only the V2F model, which has increased near wall turbulence modeling capabilities provided somewhat reliable results.

Aunapu, et al. [2000] attempted to reduce the harmful effects of secondary flows by diverting or reducing the passage vortex through the introduction of blowing along the endwall as shown in Figure 2.25. The researchers hypothesized that endwall blowing might have a similar effect to that seen in earlier work by Chung and Simon [1993] in which a fence was placed in the middle of the passage to lift the passage vortex into the mainstream. Eliminating or reducing the passage vortex could increase the film cooling effectiveness while also reducing aerodynamic losses. The researchers concluded that endwall jets located in the center of the turbine passage were effective in altering the path of the pressure side leg of the horseshoe vortex, but it was not weakened when the jets were supplied with airflow that was comparable to what would be used for film cooling holes. While the jets appeared to provide improved airfoil cooling, there were high secondary flow losses from jet turbulence.

McLean, et al [2001a, 2001b] explored and quantified the effects of coolant injection on the aerodynamic performance of the turbine for radial cooling, impingement cooling in the wheelspace cavity, and root injection, all of which is shown in Figure 2.26. Radial cooling was defined as cooling air being injected radially along the nozzle wheelspace disk, impingement cooling injected cooling air normal to the rotor disk and root injection injected cooling air at the nozzle guide vane root along the exit angle inclined at a 45° angle to the hub surface and aligned with the exit flow angle. Overall, the effects of 1% cooling air were shown to have significant implications on the performance and exit conditions of the turbine. While radial and impingement cooling showed little overall effect on the pressure coefficient, the root injection was able to cause a redistribution of the pressure coefficient data. The blowing rates being considered were said to closely match those seen in the literature. While acknowledging the thermal benefits of these leakage flows, the researchers were primarily concerned with its effect on the overall turbine efficiency.

While considerable time and resources have been spent investigating both flow and thermal characteristics within the turbine vane, considerably less work has been done looking at turbine blade geometries, specifically leakage flows and film cooling slots. Most work has focused on the upstream turbine vanes and turbine blade flows while generally disregarding most cooling in the blade region. The research presented in this thesis explores an array of leakage flows that are thought to provide cooling over the endwall, but whose overall effects are generally unknown. Leakage cooling from three different sources is considered and shown in Figure 2.27. Included in this study is cooling from: a backward facing step located upstream of the blades, cooling from the interface of two blade platforms (commonly referred to as the gutter), and leakage flows from a slot located downstream of the platform. Effectiveness predictions are made along the endwall, and thermal and flow fields throughout the passage are also presented. In addition, several microcircuits within the blade passages are also examined. The computational work presented in this thesis studies both leakage and microcircuit cooling flows and is new to the literature providing insight into realistic turbine blade platform cooling techniques.

Table 2.1. Researchers who have studied coolant blowing from the tip region.

Researcher	Year	Tip Geometry	Hole Geometry	Break-out Angle	Blowing Location
Kim and Metzger	1995	flat	slot	30°	pressure side
Kim, et al.	1995	flat	slot	90°	pressure side along tip
		flat	holes	90°	pressure side along tip
		flat	shaped holes	45°	pressure side
		squealer	holes	90°	pressure side in cavity
Kwak and Han	2002a	flat	holes	90°	pressure side along tip
		flat	holes	30°	pressure side
Kwak and Han	2002b	squealer	holes	90°	pressure side in cavity
		squealer	holes	30°	pressure side
Acharya, et al	2002	flat	holes	90°	pressure side along tip
		squealer	holes	90°	pressure side along tip

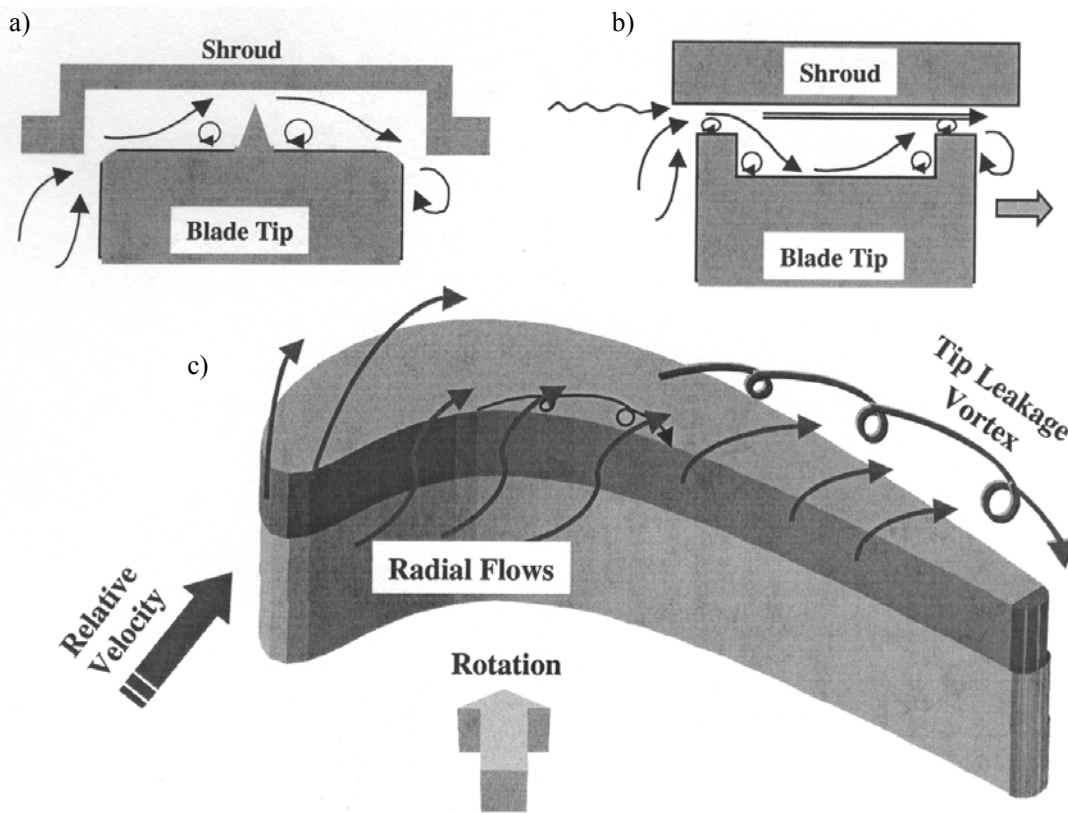


Figure 2.1a-c. Various flow features around the tip of a turbine blade showing a a) blade tip with recessed shroud, b) squealer tip and shroud, and c) flow features over the tip gap. (Bunker, 2000a).

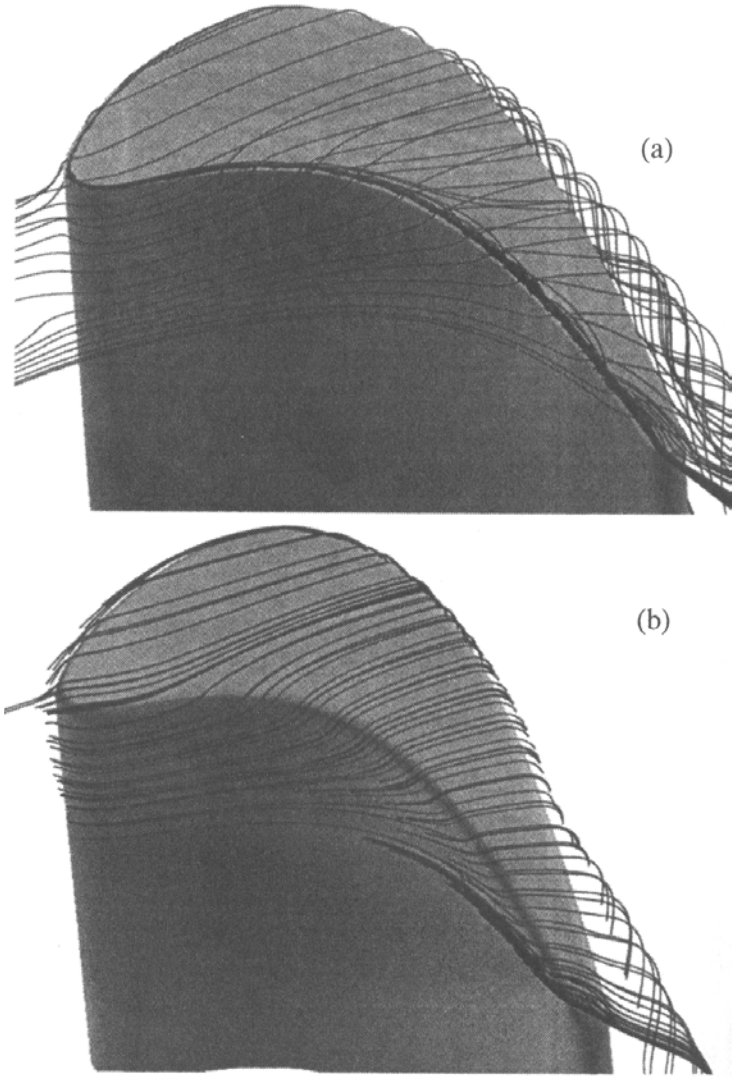


Figure 2.2a-b. Flow streamlines over the blade tip for a a) sharp edge blade tip, and b) smooth edge blade tip. (Ameri and Bunker, 2000)

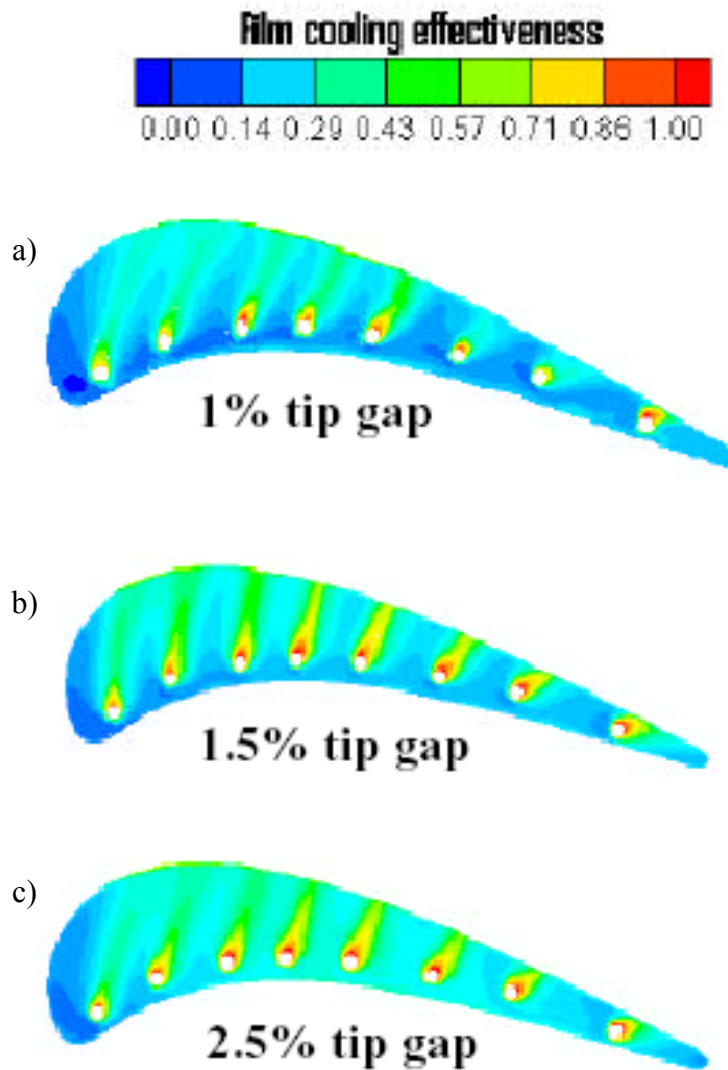


Figure 2.3a-c. Predictions of film cooling effectiveness along a flat tip for coolant injected from pressure side holes at tip gap heights of a) 1% of the blade span, b) 1.5% of the blade span, and c) 2.5% of the blade span. (Acharya, et al, 2002)

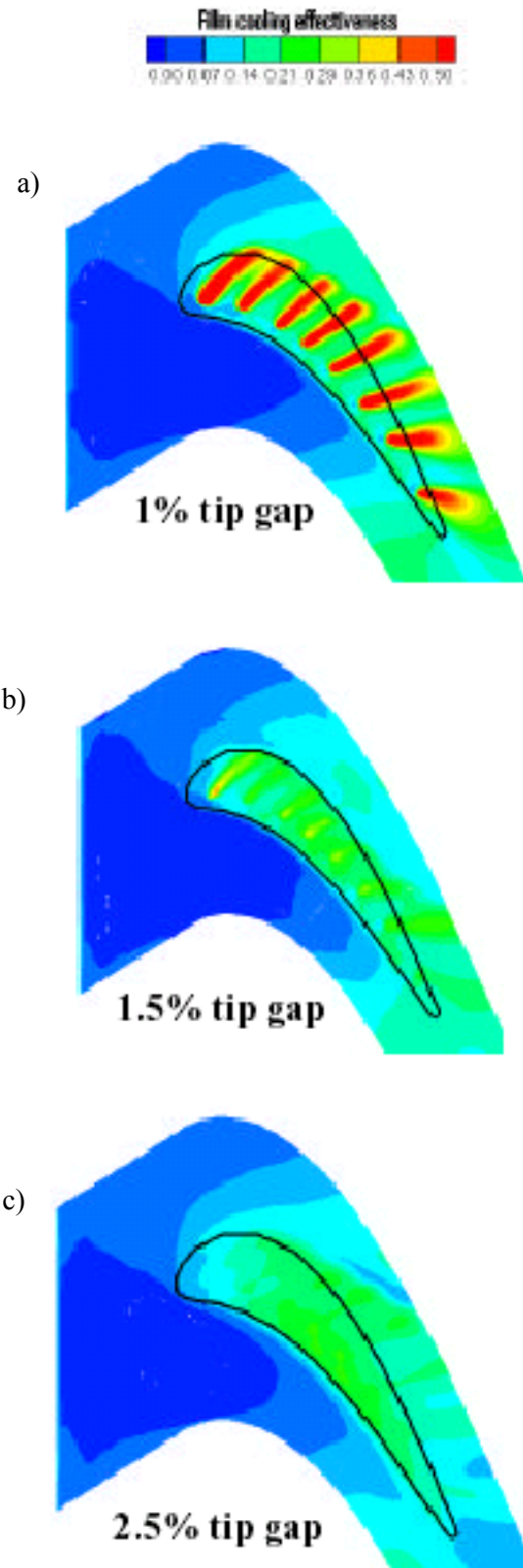


Figure 2.4a-c. . Predictions of film cooling effectiveness along the shroud for coolant injected from pressure side holes at tip gap heights of a) 1% of the blade span, b) 1.5% of the blade span, and c) 2.5% of the blade span. (Acharya, et al, 2002)

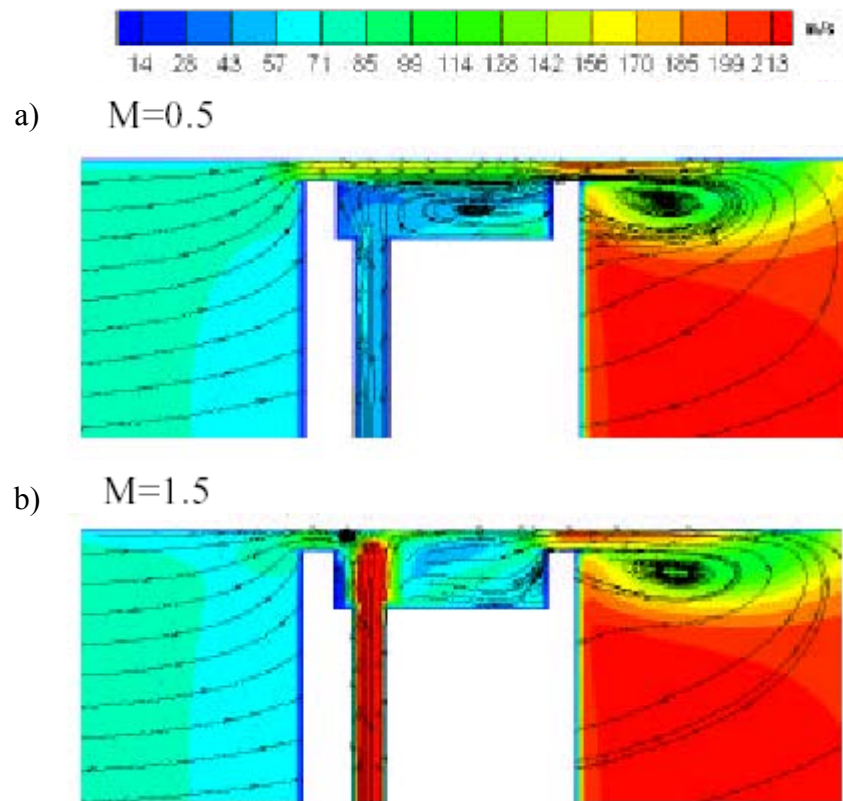


Figure 2.5a-b. Predictions of streamlines and velocity magnitude contours through a plane at the mid-chord for blowing ratios of a) $M=0.5$ and b) $M=1.5$. (Acharya, et al, 2002)

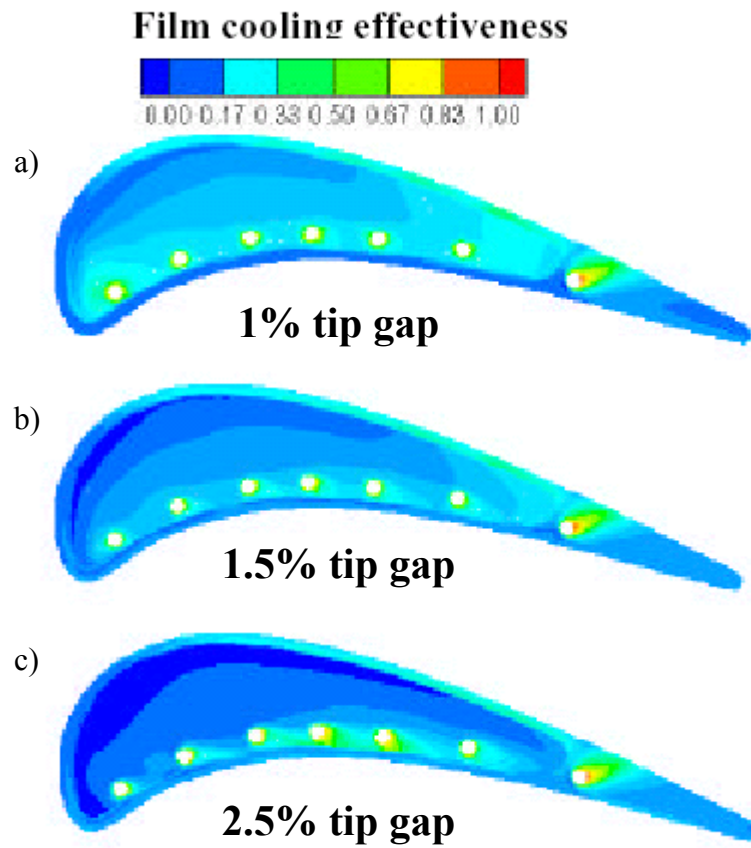
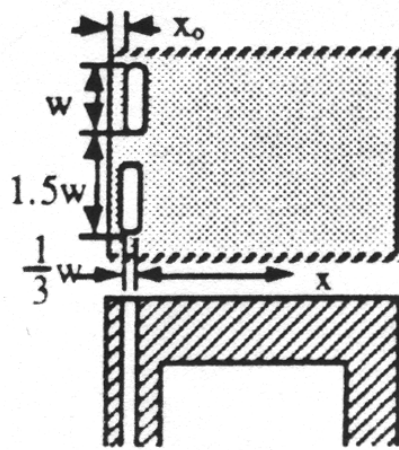
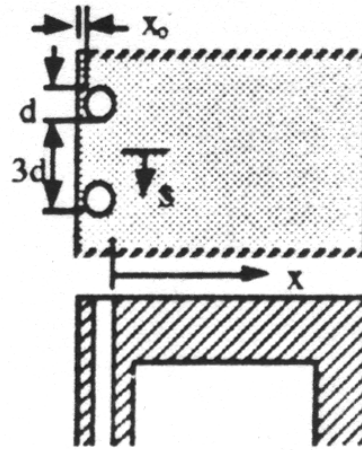


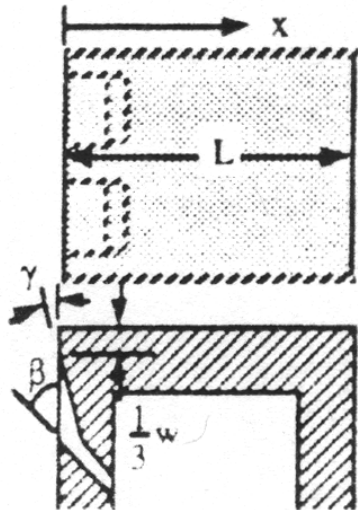
Figure 2.6a-c. Predictions of film cooling effectiveness along a squealer tip for coolant injected from pressure side holes at tip gap heights of a) 1% of the blade span, b) 1.5% of the blade span, and c) 2.5% of the blade span. (Acharya, et al, 2002)



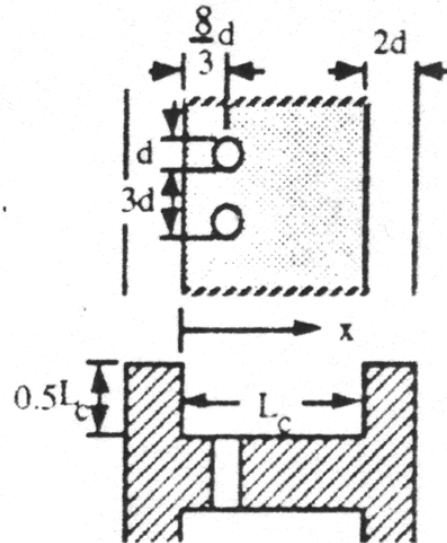
(a) Discrete Slot



(b) Round Hole



(c) Pressure Side



(d) Grooved-Tip

Configuration	Dimensions (cm)
Discrete Slot	$x_0=0.25, w=0.95$
Round Hole	$x_0=0.25, d=0.48$
Pressure Side	$w=0.95, \gamma=12^\circ, \beta=45^\circ$
Grooved Tip	$d=0.48, L_c=5.08$

Figure 2.7a-d. Four different blade tip geometries studied by Metzger to examine variations in heat transfer coefficients including a) discrete slots, b) round holes, c) pressure side injection, and d) grooved tips. (Kim, et al, 1995)

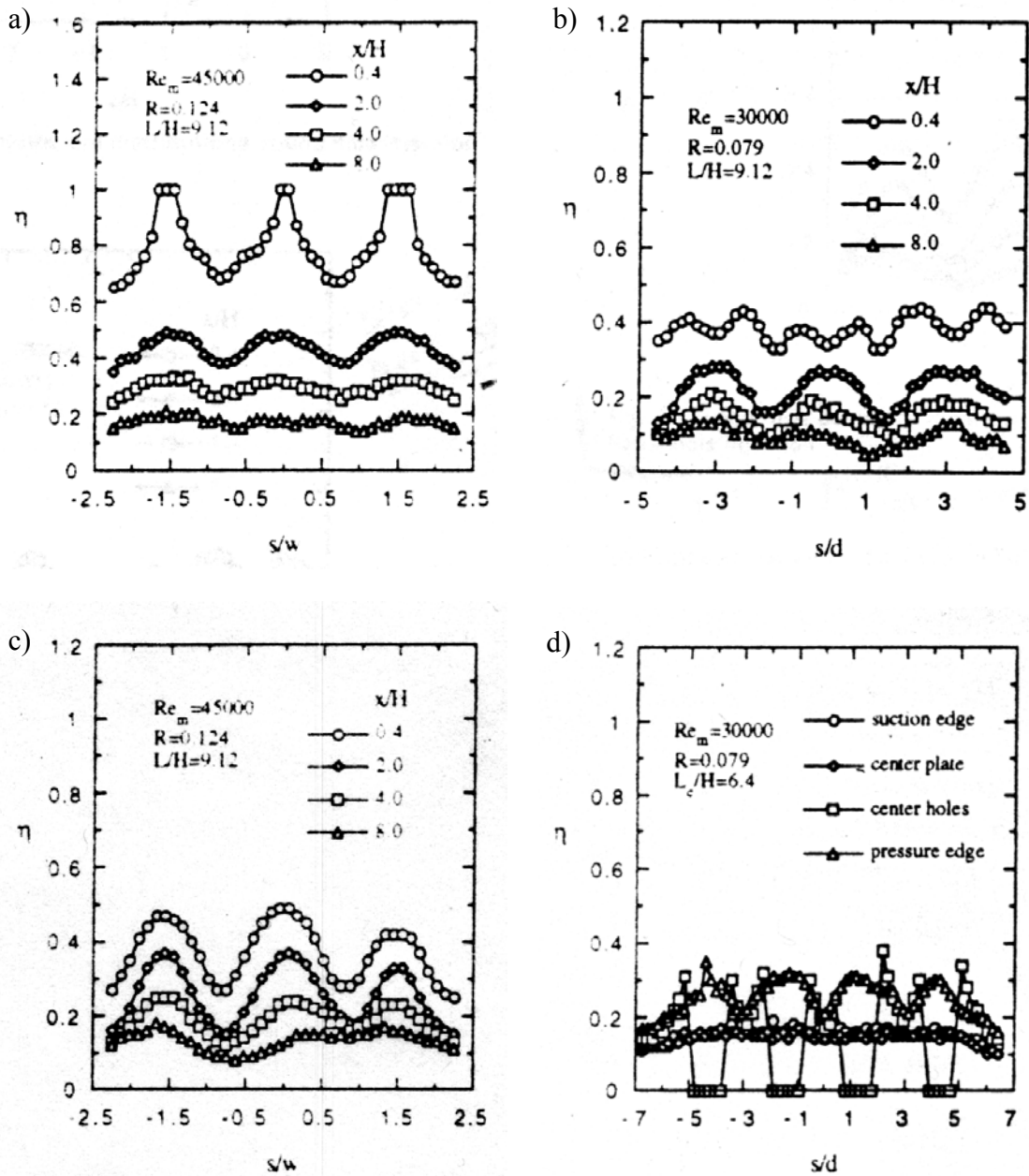


Figure 2.8a-d. Typical spanwise film cooling effectiveness results at various locations downstream of the cooling ducts for a) discrete slots, b) round holes, c) pressure side injection, and d) grooved tips. (Kim, et al, 1995)

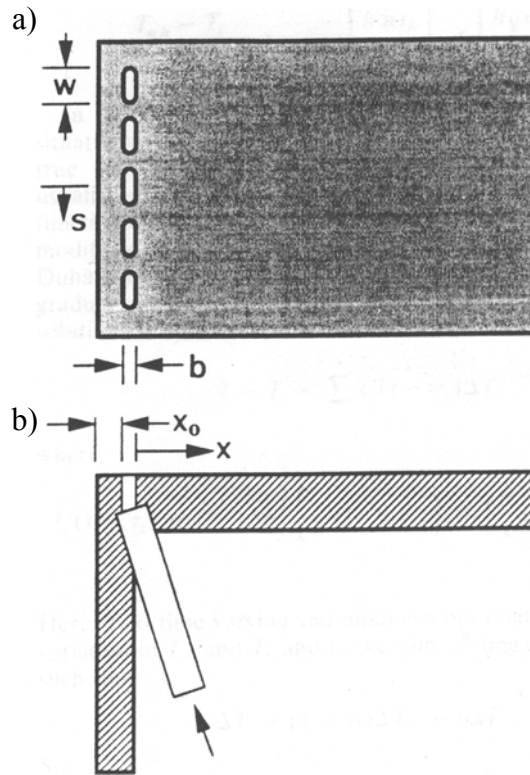


Figure 2.9a-b. Film cooling hole configuration used by Kim and Metzger to look at cooling effectiveness and heat transfer coefficients shown from a) top and b) side views. (Kim and Metzger, 1995)

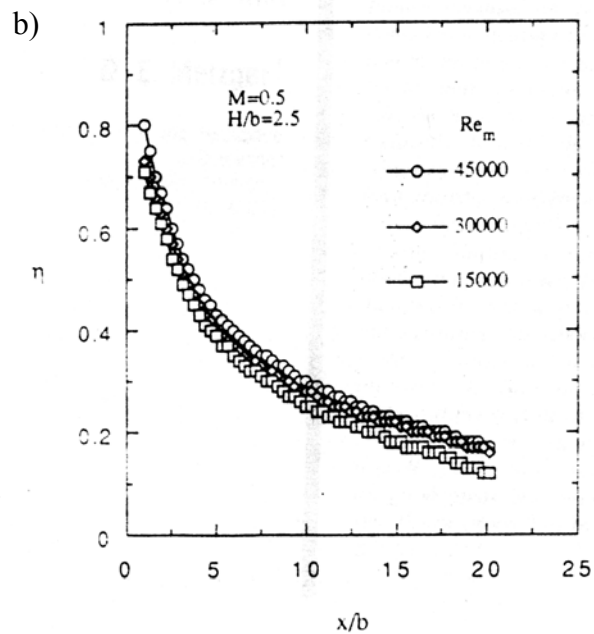
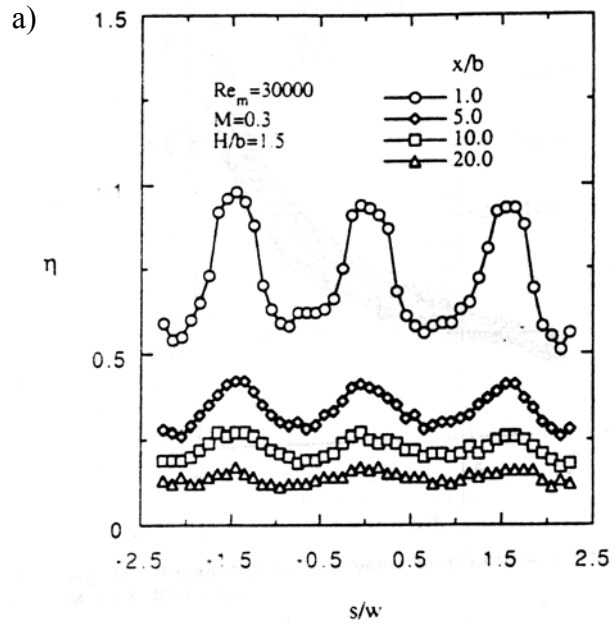


Figure 2.10a-b. Film cooling effectiveness measurements a) shown downstream of film cooling slots, and b) averaged across the span for a blowing ratio of $M=0.5$ at three different Reynolds numbers. (Kim and Metzger, 1995)

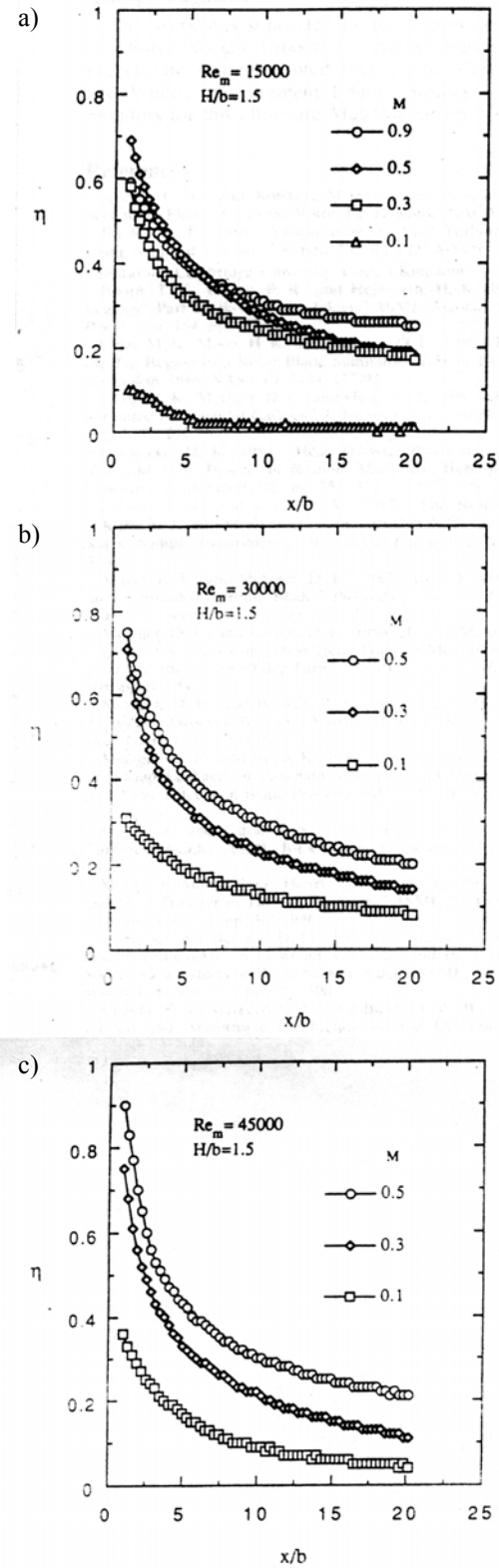


Figure 2.11a-c. Spanwise averaged effectiveness for a) $Re=15,000$ at four blowing ratios, b) $Re=30,000$ at three blowing ratios, and c) $Re=45,000$ at three blowing ratios. (Kim and Metzger, 1995)

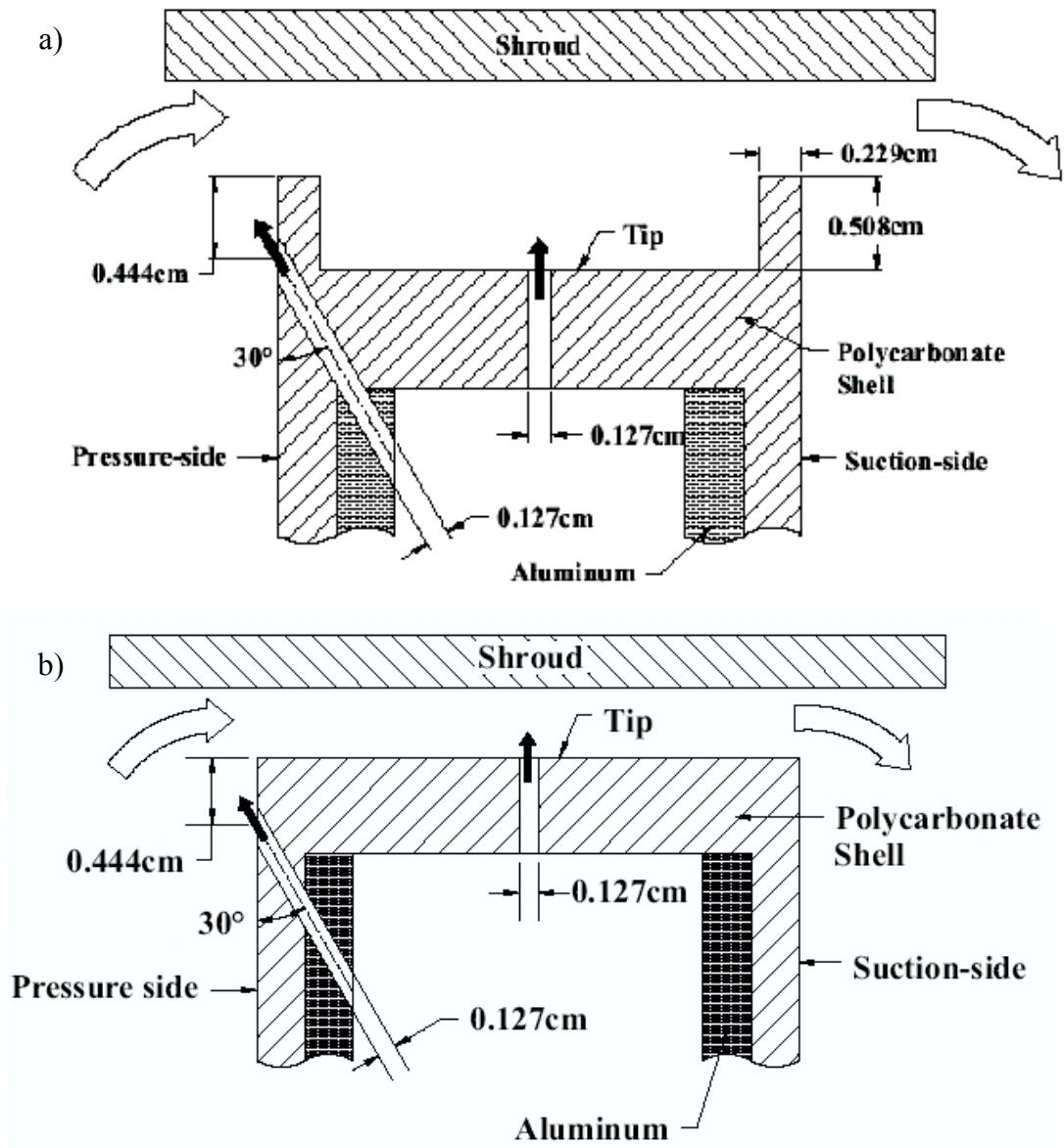


Figure 2.12a-b. Film-cooling configurations shown a) with a squealer tip (Kwak and Han, 2002b) and b) flat tip (Kwak and Han, 2002a).

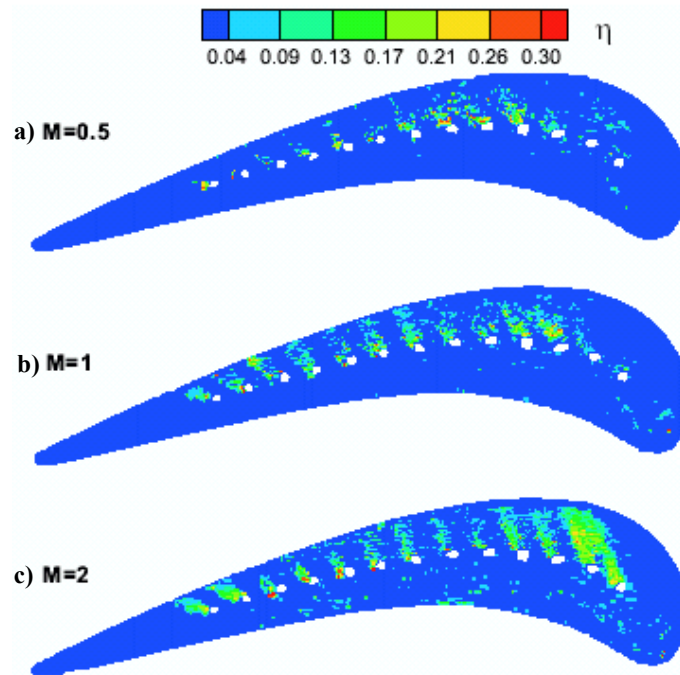


Figure 2.13a-c. Film cooling effectiveness contours for tip blowing over a flat tip having a 1.5% tip gap with blowing ratios of a) $M=0.5$, b) $M=1$, and c) $M=2$. (Kwak and Han, 2002a)

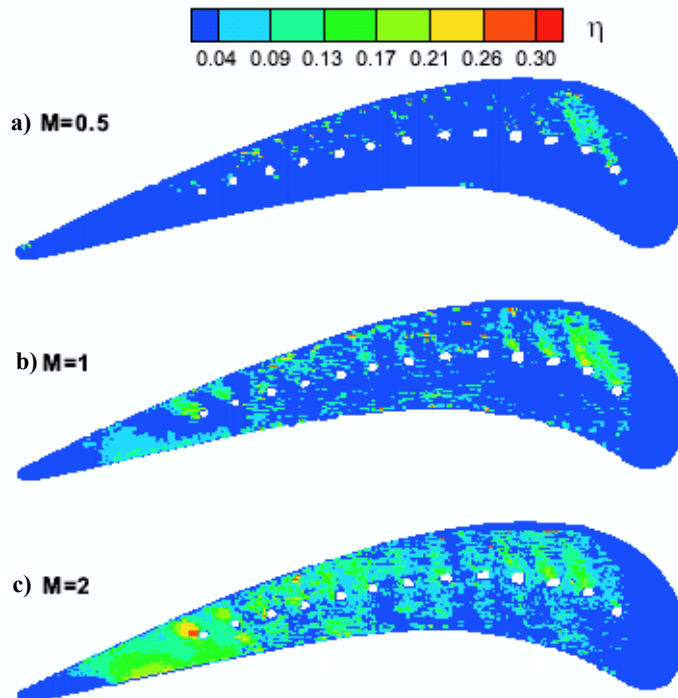


Figure 2.14a-c. Film cooling effectiveness contours for tip and pressure side blowing over a flat tip having a 1.5% tip gap with blowing ratios of a) $M=0.5$, b) $M=1$, and c) $M=2$. (Kwak and Han, 2002a)

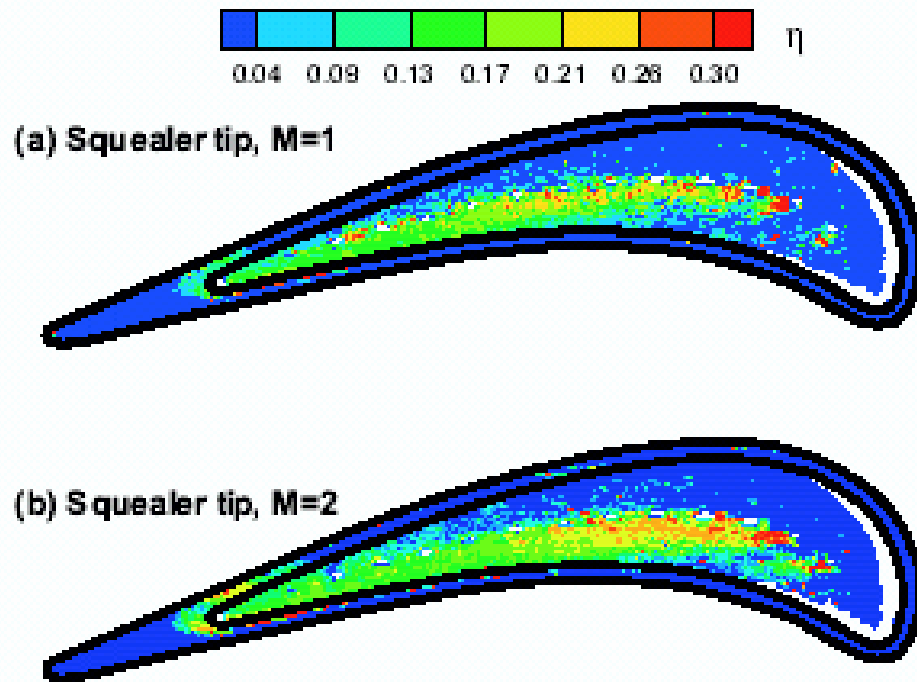


Figure 2.15a-b. Film cooling effectiveness contours for tip blowing over a squealer tip having a 1.5% tip gap with blowing ratios of a) $M=1$, and b) $M=2$. (Kwak and Han, 2002b)

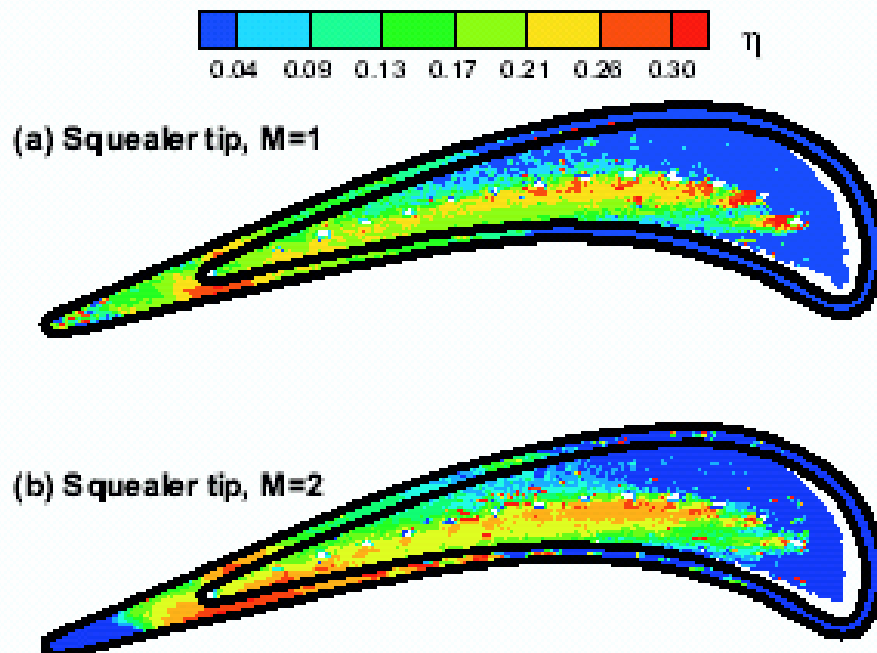
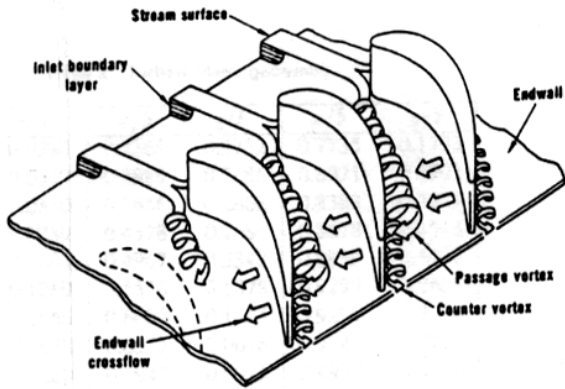
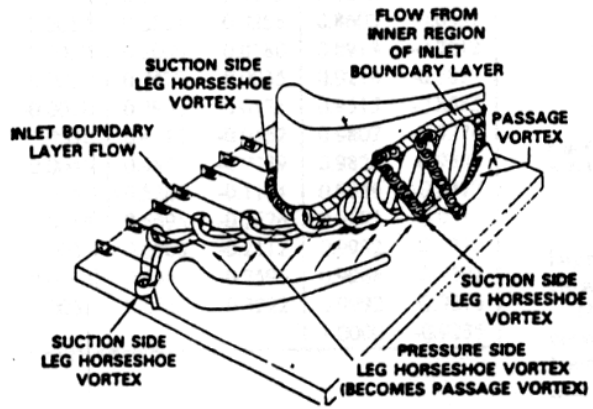


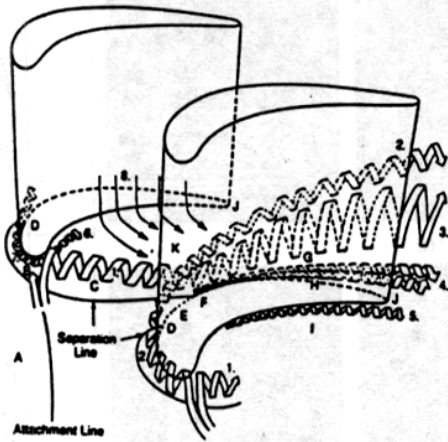
Figure 2.16a-b. Film cooling effectiveness for tip and pressure side blowing over a squealer tip having a 1.5% tip gap with blowing ratios of a) $M=1$, and b) $M=2$. (Kwak and Han, 2002b)



(a) Vortex pattern described by Langston (1980).



(b) Vortex pattern described by Sharma and Butler (1987).



(c) Vortex pattern described by Goldstein and Spores (1988).

Figure 2.17. Turbine flow patterns as defined by a) Langston [1980], b) Sharma and Butler [1987], and c) Goldstein [1988].

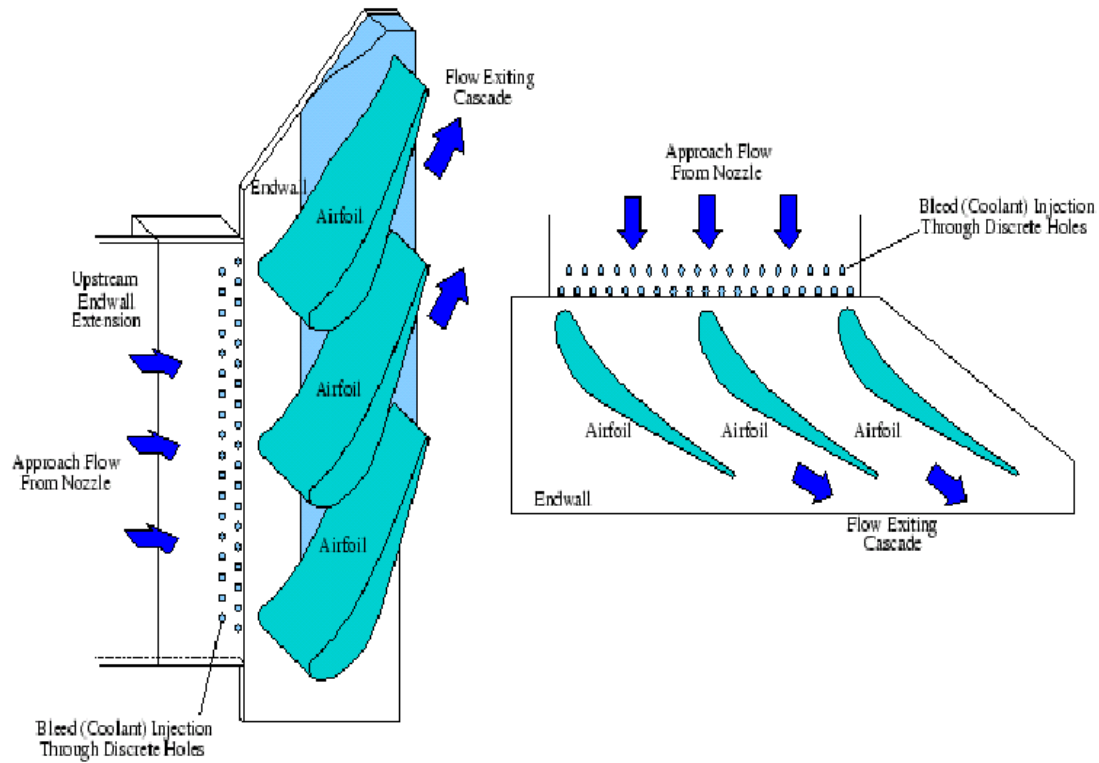


Figure 2.18. Cooling holes located upstream of first stage turbine vane as studied by Oke. (Oke, et al, 2000)

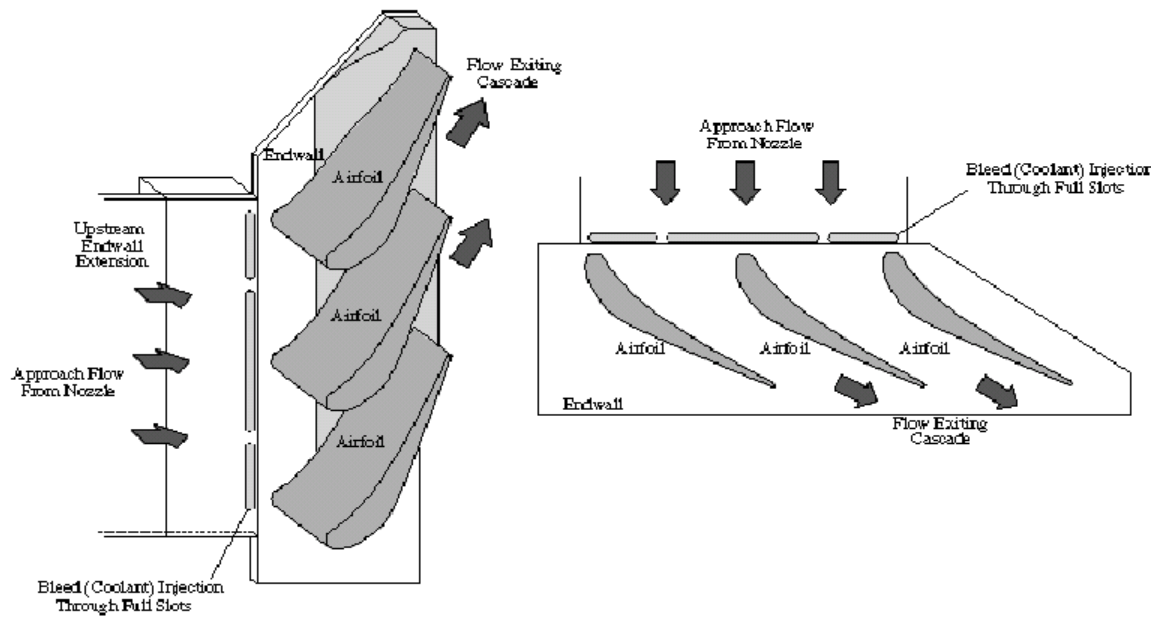


Figure 2.19. Upstream slot configuration for tests run by Burd. (Burd, et al, 2000)

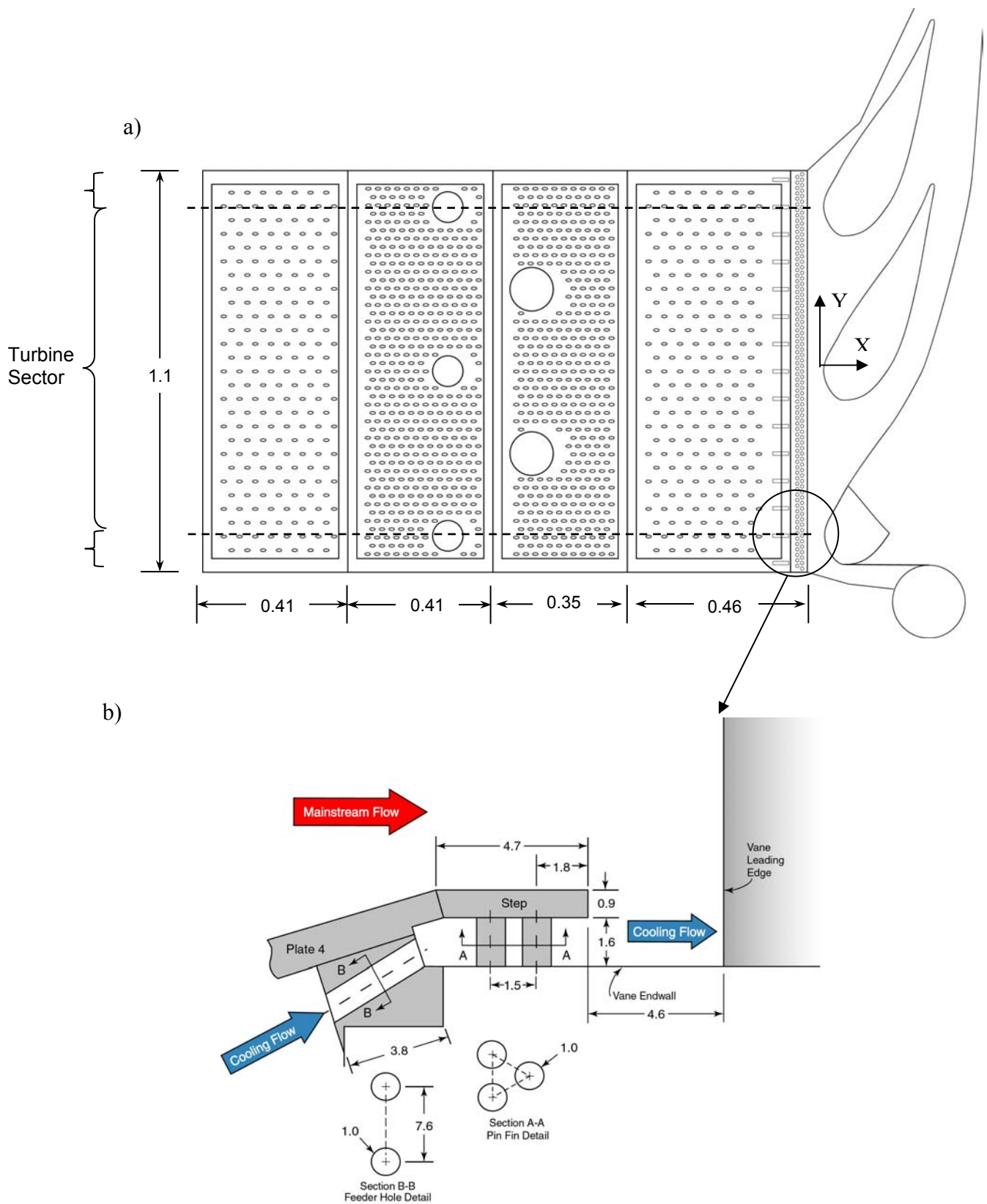


Figure 2.20a-b. Diagram of experimental test configuration for Colban and Tholes slot and film cooling work oriented a) looking down at film-cooling holes, dilution jets and slot and b) detailed cross-sectional view of slot configuration. (Colban and Thole, 2003)

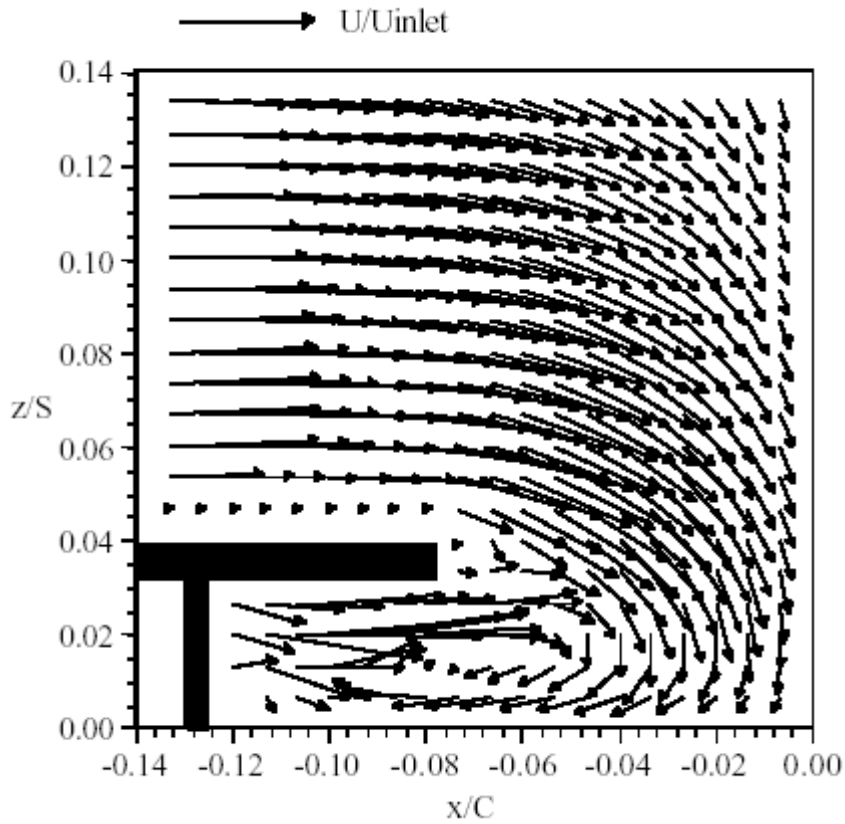
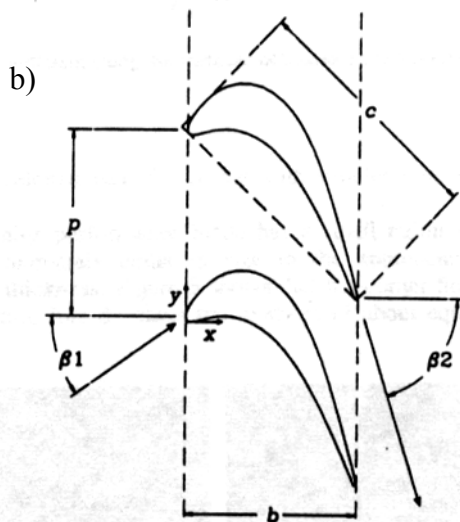
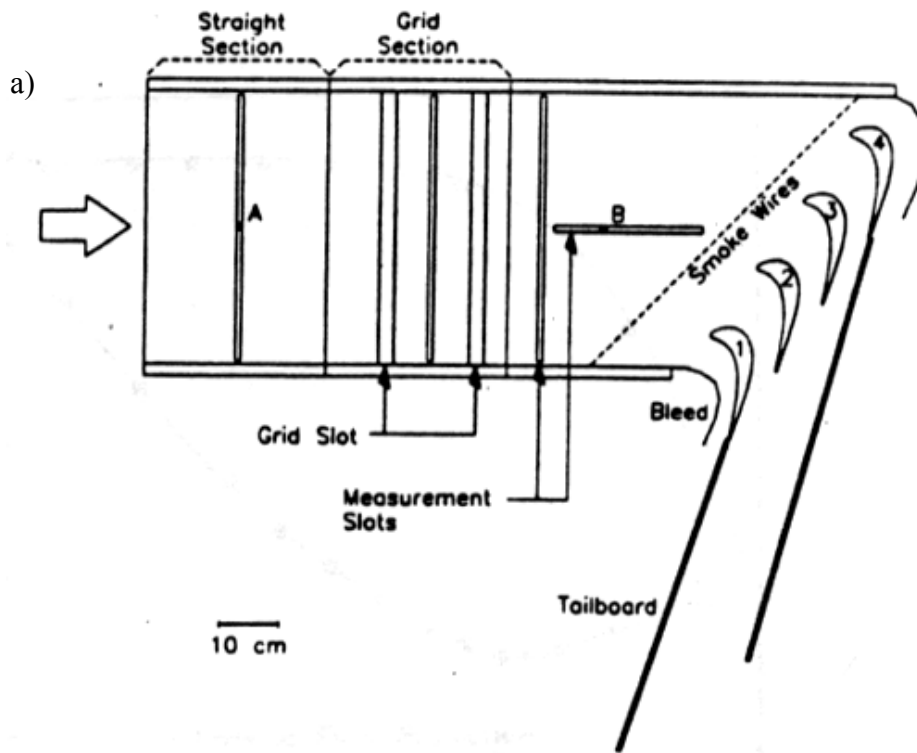


Figure 2.21. Step configuration computationally examined by Stitzel and experimentally tested by Colban showing ingestion into the backward facing step. (Stitzel, 2001)



Number of blades	4
Chord length of blade - c	184.15 mm
Axial Chord to Chord ratio - b/c	0.704
Pitch to Chord ratio - p/c	0.750
Aspect ratio (Span/Chord) - l/c	2.483
Blade inlet angle - β_1	35°
Blade outlet angle - β_2	-72.49°
Incoming Velocity - U_{in}	0.80 m/s
Exit Velocity - U_{ex}	2.18 m/s
Reynolds Number - Re_{ex} (for all flow visualization)	2.7×10^4

Figure 2.22a-b. Views of a) experimental test facility, and b) detailed blade geometry. (Wang, et al, 1997)

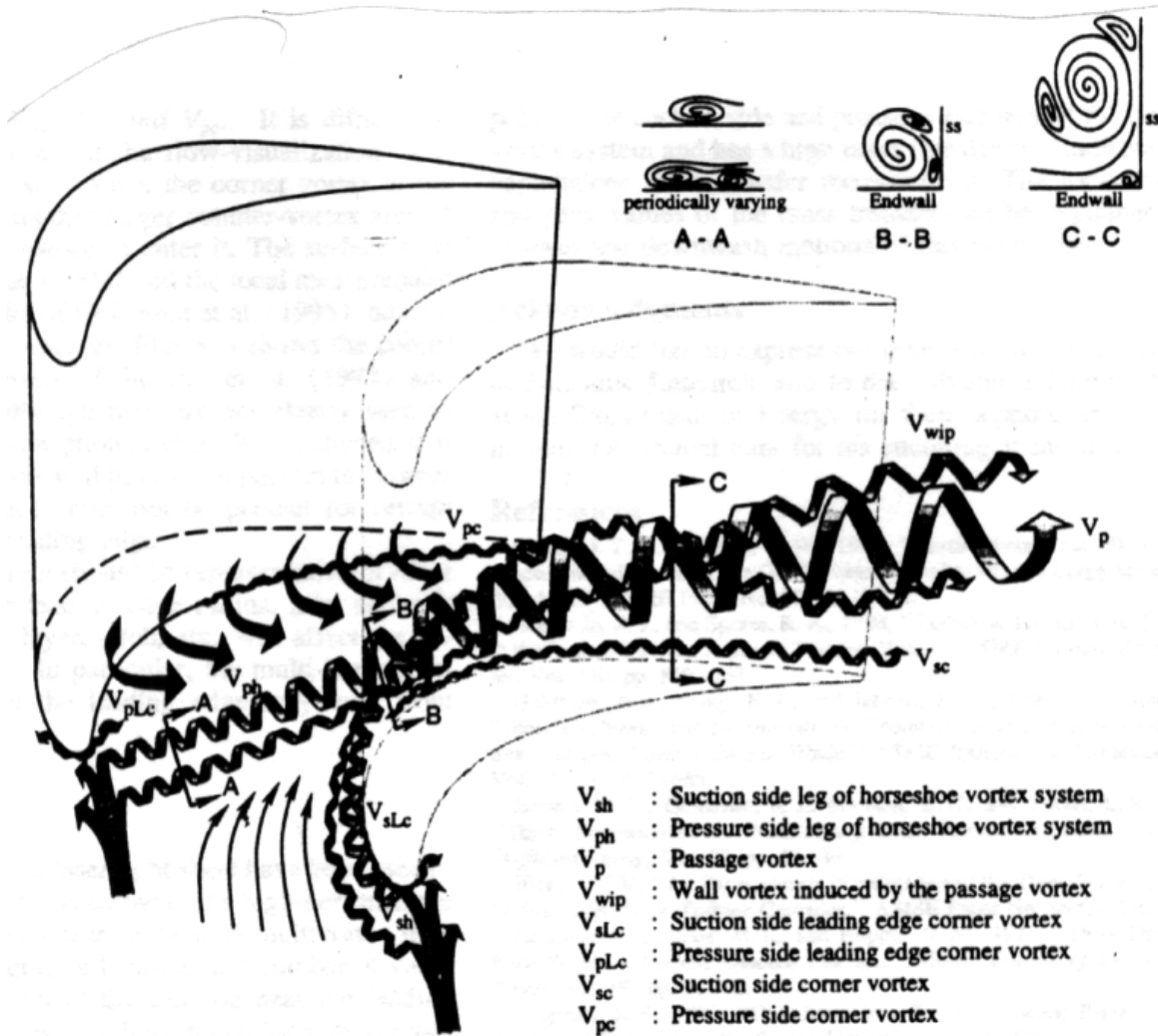


Figure 2.23. Proposed flow patterns within a turbine blade cascade. (Wang, et al, 1997)

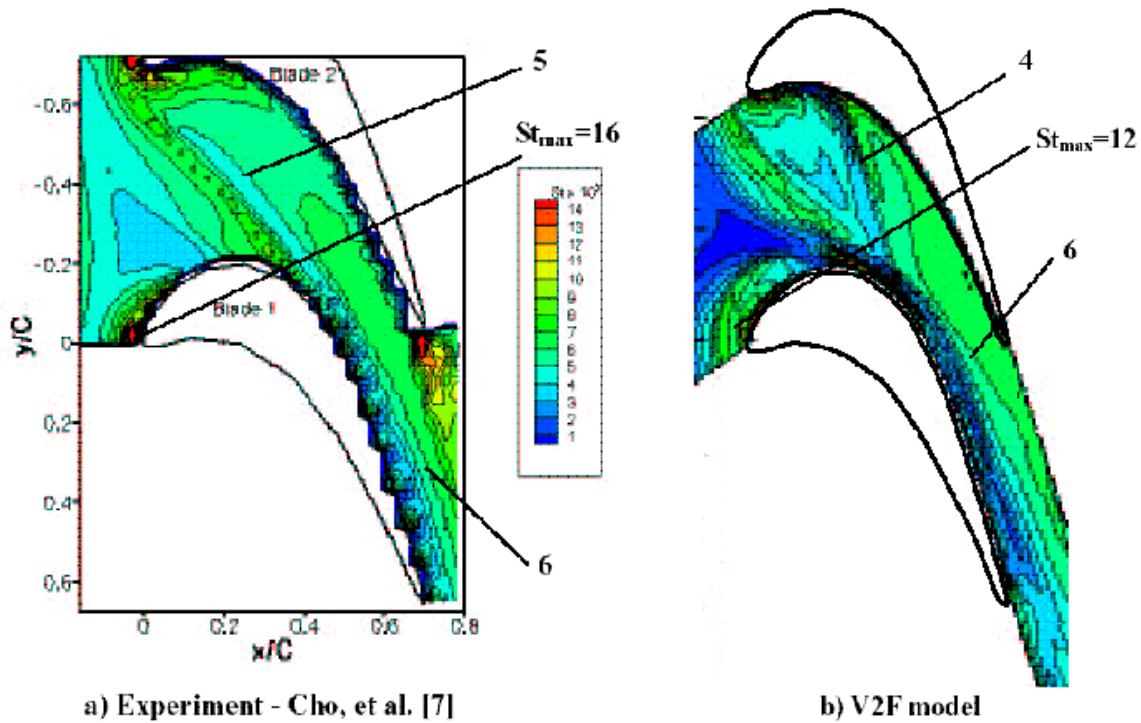


Figure 2.24a-b. Contours of Stanton number along the endwall for the rotor blade geometry. (Hermanson, et al, 2002)

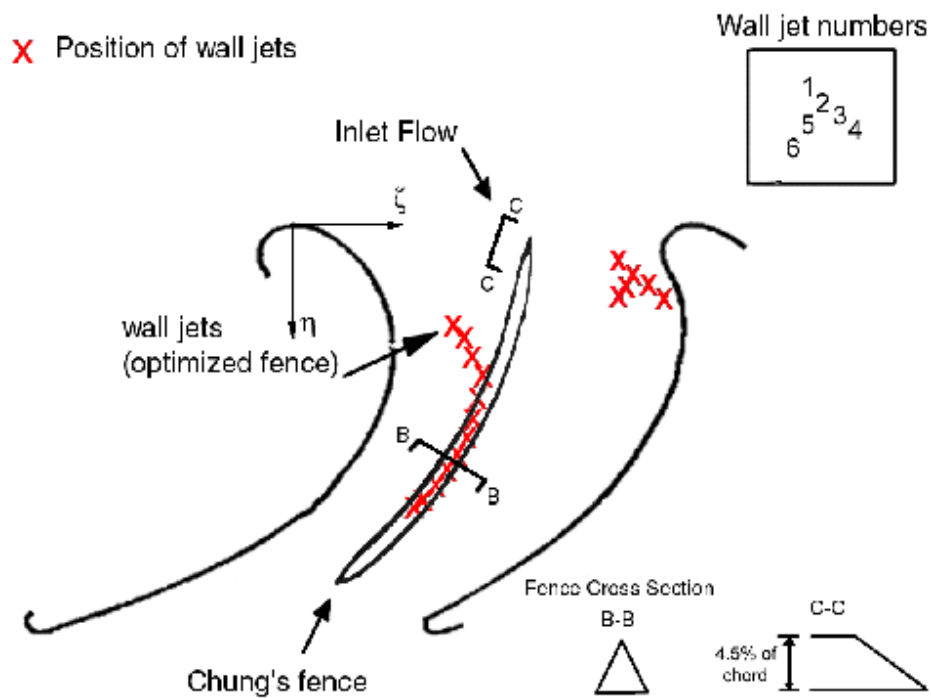


Figure 2.25. Top view of the experimental test section showing flow control schemes: location of endwall fence as used by Chung and Simon (1993); location of upstream jets (1-5) and location of optimized boundary layer fence. (Anapu, et al, 2000).

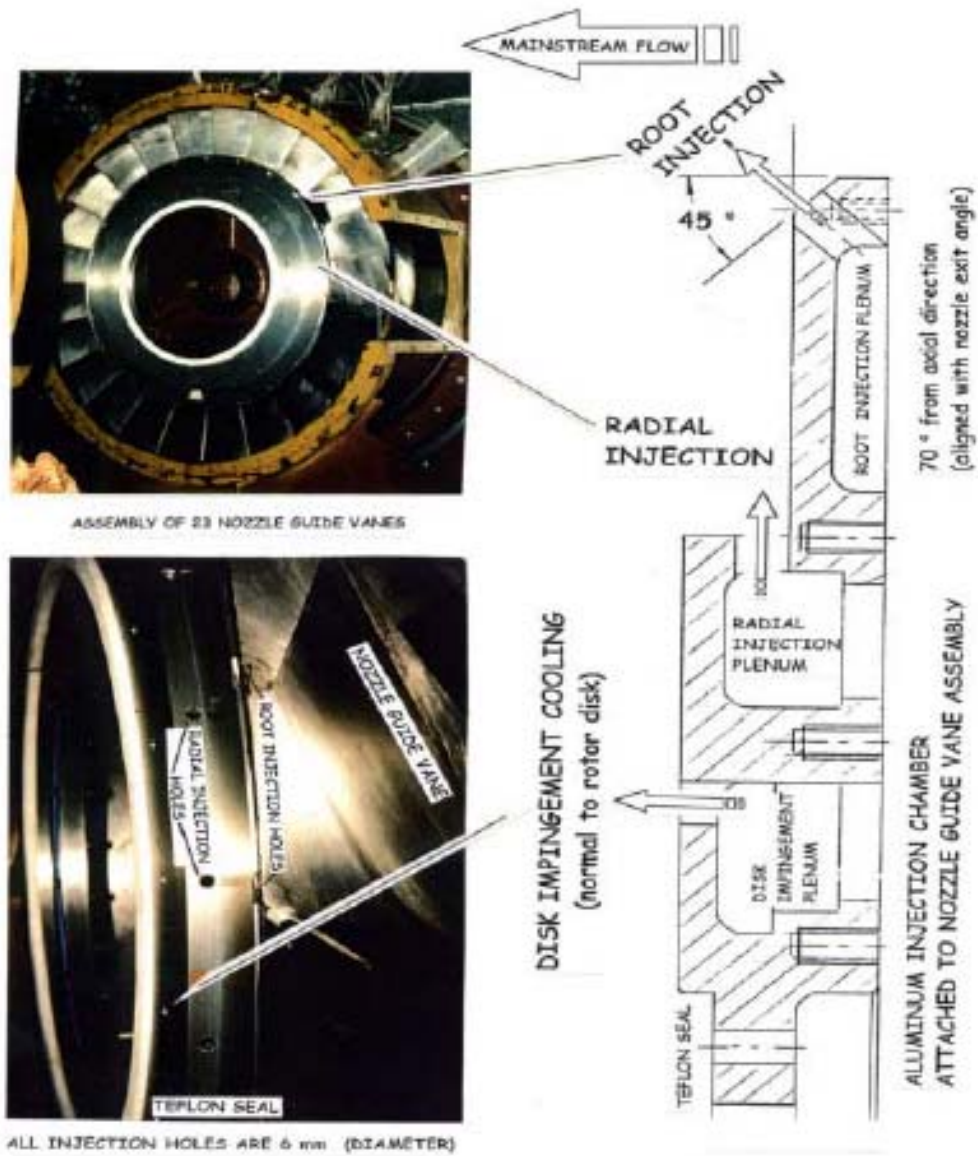


Figure 2.26. Cooling flow injection chambers for radial cooling, impingement cooling and root injection. (McLean, et al, 2001a, 2001b)

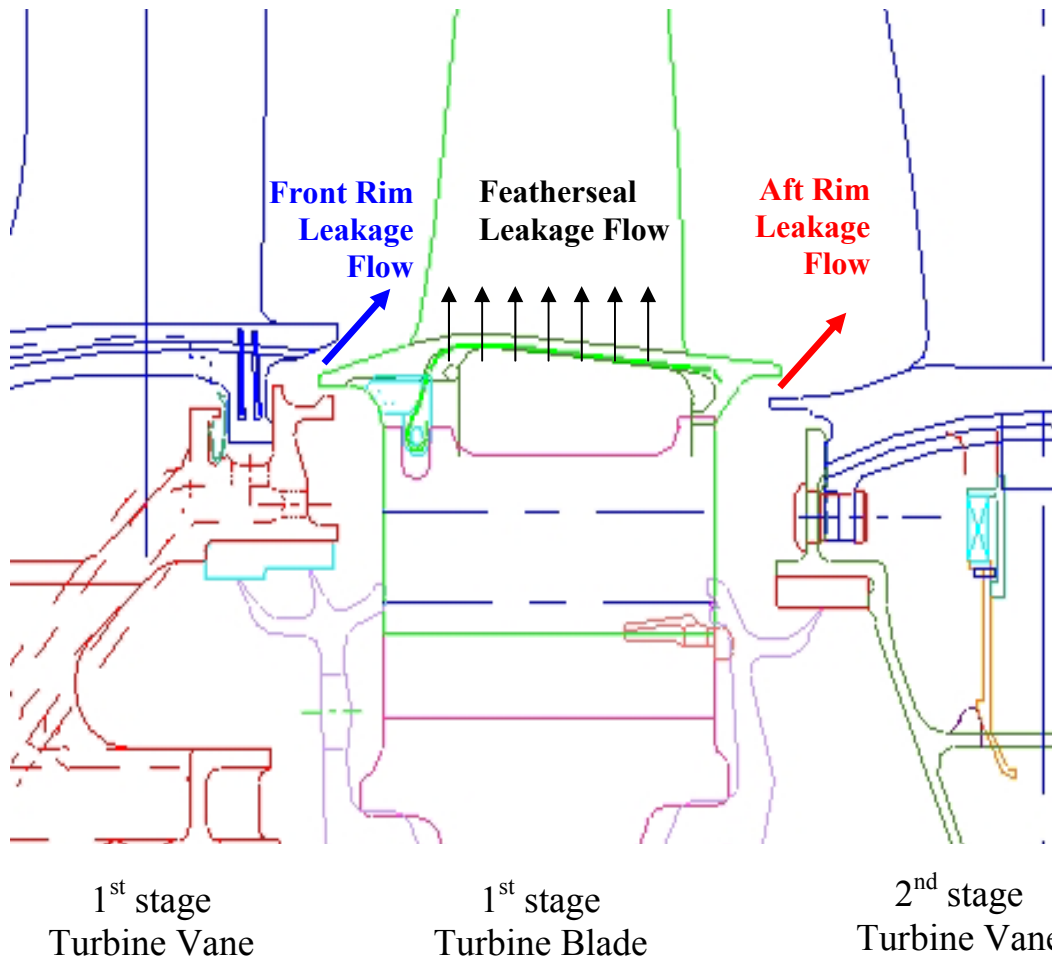


Figure 2.27. Realistic engine leakage flows in a first stage turbine blade (courtesy Pratt and Whitney, 2002).